

# Models of Chemistry, Thermal Balance, and Infrared Spectra from Intermediate-Aged Disks around G and K Stars

U.Gorti

*University of California, Berkeley, CA*

D.Hollenbach

*NASA Ames Research Center, Moffett Field, CA*

## ABSTRACT

We model gas and dust emission from regions 0.3–20 AU from a central low mass star in intermediate-aged ( $\sim 10^7$  years) disks whose dust is fairly optically thin to stellar radiation. The models treat thermal balance and chemistry self-consistently, and calculate the vertical density and temperature structure of the gas in a disk. The gas and dust temperatures are calculated separately. The models cover gas masses  $10^{-3} - 1 M_J$ , dust masses  $10^{-7} - 10^{-4} M_J$ , and treat solar type (G and K) stars. We focus on mid-infrared and far-infrared emission lines from various gas species such as the rotational lines of H<sub>2</sub>, OH, H<sub>2</sub>O and CO molecules and the fine structure lines of carbon, oxygen, sulfur, iron, and silicon atoms and ions. These lines and the dust continuum are observable by the Spitzer Space Telescope, and future missions including SOFIA and the Herschel Space Observatory. We find that the [SI]25.23 $\mu$ m line is the strongest emission line for a wide range of disk and stellar parameters, followed by emission from [SiII]34.8 $\mu$ m, [FeII]26 $\mu$ m, and [OI]63 $\mu$ m. [FeI]24 $\mu$ m and rotational lines of OH and H<sub>2</sub>O are strong when gas masses are high ( $\gtrsim 0.1 M_J$ ). Emission from the rotational lines of H<sub>2</sub> is more difficult to detect, unless disk gas masses are substantial ( $\gtrsim 0.1 M_J$ ). For emission from H<sub>2</sub> lines to be observable and yet the dust be optically thin in stellar light, the ratio of gas to small sub-millimeter sized dust particle mass in the disk needs to be  $\gtrsim 1000$ , or at least an order of magnitude higher than that in the interstellar medium. This may be possible at intermediate stages in disk evolution, such as in the gas gathering stage of the core accretion scenario for giant planet formation, where most of the dust has coagulated into larger objects ( $\gg 1\text{mm}$ ) but the gas has not yet fully dispersed. Whereas the absolute fluxes observed in some lines such as [FeI]24 $\mu$ m and H<sub>2</sub> S(0) 28 $\mu$ m primarily measure the gas mass in the disks, various line ratios diagnose the inner radius of the gas, and the radial temperature and surface density distribution of the gas. Many

lines become optically thick and/or suffer chemical or thermal effects such that the line luminosities do not increase appreciably with increasing gas mass. We predict it may be difficult for the Spitzer Space Telescope to detect  $\lesssim 1 M_J$  of gas in optically thin (in dust) disks at distances  $\gtrsim 150$  pc. The models presented here will be useful in future infrared studies of the timescale for the dispersion of gas in a planet-forming disk, and testing core accretion models of giant planet formation.

*Subject headings:* infrared: spectra — planetary systems: protoplanetary disks — stars: circumstellar matter — stars: formation

## 1. Introduction

Circumstellar disks evolve from gas-rich structures with 1% of the total mass in dust to disks which are observed to be completely devoid of gas and dominated by emission from dust particles. During this process of evolution, the disk, which is initially very optically thick in dust with radial midplane optical depths in the visual  $\tau_V \gtrsim 10^3$ , becomes optically thin with  $\tau_V \sim 1$  in a few million years (Haisch, Lada & Lada 2001). At this intermediate stage of disk evolution planetary formation is probably underway with dust particles colliding and growing to form larger objects (which greatly reduces  $\tau_V$ ), and with some residual gas. Disks with ages  $\gtrsim 10^7$  years are observed to have almost no gas (Zuckerman et al. 1995; Duvert et al. 2000). Smaller dust particles in these disks have either dispersed or have coagulated to larger sizes, and these disks are very optically thin in dust with  $\tau_V \lesssim 10^{-2}$ . These very optically thin disks are called “debris disks”, as the dust in these disks is generally not primordial but is continually generated debris from colliding rocky bodies and planetesimals.

The evolution of the dust component of disks has been extensively studied (e.g., Weidenschilling 1977; Weidenschilling et al. 1997) in models where the dust grains in disks grow in size via collisional agglomeration. As dust grains grow and planetesimals eventually form, the disk becomes optically thin to stellar radiation and the fractional dust luminosity,  $f_D = L_{IR}/L_{bol}$ , the ratio of the disk infrared luminosity to the stellar bolometric luminosity, is observed to decrease with the age of the disk as  $t^{-1.76}$  (Habing et al. 1999; Spangler et al. 2001; Zuckerman 2001). This decrease in dust luminosity occurs as micron-sized or smaller particles are lost through the effects of radiation pressure, Poynting-Robertson drag and collisions (e.g., Backman & Paresce 1993), and the population of larger bodies which are the ultimate source of the dust dwindles.

Gas evolution in disks is less well understood. CO observational studies seem to indicate

that gas beyond about 30 AU disappears rather abruptly at disk ages  $\gtrsim 10^7$  years (e.g., Zuckerman et al. 1995; Duvert et al. 2000). Theoretical studies also indicate short gas dispersal timescales (Hollenbach, Yorke & Johnstone 2000; Clark, Gendrin & Sotomayor 2001). However, there is some controversy regarding the presence or absence of gas in disks of ages  $\sim 10^7$  years. Seemingly contradicting the CO observations, there may have been detection of  $\sim 0.1 - 1 M_J$  of molecular hydrogen gas in three younger (ages  $\gtrsim 10^7$  years) debris disks by Thi et al. (2001) using ISO. These ISO results are controversial (see LeCavalier des Etangs et al. 2001; Richter et al. 2002; Sheret et al. 2003; Brandeker et al. 2004). If the ISO observations are confirmed, then perhaps CO is not a reliable tracer of gas mass in such systems, and may be subject to chemical effects such as freezing onto cold dust grain surfaces in the outer disks and optical depth effects in the inner disk. On theoretical grounds, although gas in the outer regions ( $r \gtrsim 10 - 100$  AU) may be subject to photoevaporation due to stellar radiation, gas inside these radii does not photoevaporate because it is more tightly bound gravitationally to the star. Viscous accretion onto the central star and viscous spreading to the outer photoevaporating disk likely dominates the gas dispersal of the inner ( $r \lesssim 10 - 100$  AU) disk (Johnstone et al. 1998; Hollenbach et al. 2000; Clarke et al. 2001). However, the timescale for viscous dispersal at  $r \sim 10 - 100$  AU is uncertain.

A determination of gas dispersal timescales in disks is important for understanding the formation of planetary systems. Two competing theories exist for the formation of gas giants. Gaseous Jovian-type planets are believed to form in disks via accretion of gas onto rocky cores of a few earth masses (e.g., Lissauer 1993; Pollack et al. 1996; Kornet, Bodenheimer & Rozyczka 2002) or by gravitational instability in disks leading to the formation of clumps which subsequently contract to form giant planets (e.g., Boss 2003). The presence or absence of gas in intermediate-aged or transitional disks ( $\tau_V \sim 1$ , ages  $\sim 10^7$  years) can potentially discriminate between these two theories. In the gravitational instability scenario, gas giants form quickly and the gas may dissipate rapidly. Longer gas disk lifetimes ( $\gtrsim 10^6$  years) facilitate the formation of gas giant planets through conventional core accretion models, allowing sufficient time for the building of a rock/ice core of a few  $M_\oplus$  and subsequent accretion of gas. At the gas accretion stage, there would be little dust (or equivalently, particles small enough to significantly radiate at infrared/sub-millimeter wavelengths and be observed) in the gas giant regions of disks, and substantial amounts ( $\gtrsim 1 M_J$ , or a Jupiter mass) of gas. Core accretion theory suggests that systems may reside in this state for a significant length of time (few Myr, e.g., Pollack et al. 1996). At this stage, the ratio of gas mass to dust mass (where dust is defined as particles with sizes  $\lesssim 1$  mm) would initially increase from the interstellar value of 100 before the final gas dispersal reduces the ratio to values  $\ll 100$  characteristic of the older debris disks. The detection of gas infrared emission

during this epoch of gas accretion onto rock/ice cores would help support the core accretion scenario. Conversely, if very little gas ( $\ll 1 M_J$ ) is present at the moment when the dust disk first becomes optically thin (signalling the buildup of several earth mass cores), then the core accretion model is likely invalid.

In the terrestrial planet region of the disk, the residual gas content of the disk at the epoch when embryos or protoplanets assemble to form terrestrial planets helps determine the ultimate mass and eccentricity of the planet, and therefore the eventual habitability of the planet (Agnor & Ward 2002; Kominami & Ida 2002; Kominami & Ida 2004). In particular, a finite range of gas masses produces earth-mass planets on circular orbits. If the gas mass inside 3 AU at ages of  $10^{6.5}$  to  $10^7$  years is  $\gg 10^{-2} M_J$ , the tidal interaction of the planets with the gas is sufficient to circularise the orbits of lunar-mass protoplanets, making it difficult for collisions between them to build earth-mass planets. On the other hand, if the gas inside 3 AU is  $\ll 10^{-2} M_J$ , earth-mass planets can be produced, but in orbits considerably more eccentric than that of the Earth.

At later debris disk stages,  $t \gg 10^7$  years, the presence of even small amounts of gas ( $\sim 10^{-2} M_J$ ) can affect dust dynamics because of the drag forces they induce and, therefore, this gas may affect the disk structure significantly. This effect weakens the interpretations of gaps and ring signatures observed in dusty disks as being due to the presence of planets, as the presence of gas could give rise to the same structures (Klahr & Lin 2001; Takeuchi & Artynowicz 2001; Takeuchi & Lin 2002).

In the work presented here, we model gas emission from a disk that has optically thin or marginally optically thick ( $\tau_V \lesssim 5$ ) dust,<sup>1</sup> so is perhaps at a stage where considerable rock/ice planetesimal and planet formation has already taken place, but may still retain appreciable amounts (from  $\sim 10^{-3} M_J$  to  $\gtrsim 1 M_J$ ) of gas left over from the rock/ice planet building phase. We predict expected emission from such a range of gas masses in optically thin dust disks as a function of the gas mass, dust mass, and stellar properties. The results will aid future observational programs that plan to look for gas emission in disks in order to understand the evolution of gas in disks, the timescales for gas dispersal, and the process of giant planet formation. New observational facilities such as the Spitzer Space Telescope, SOFIA and the Herschel Space Observatory are sensitive enough to detect infrared and sub-millimeter emission from small amounts of gas using tracers other than CO. These IR tracers may be better suited than CO for detecting gas in the 1 AU – 20 AU planet forming region around solar-type stars. The possibility of detection of gas emission from the planet-forming

---

<sup>1</sup>Henceforth, we shall call our models “optically thin” even though as discussed in §2.1, they apply for  $\tau_V \lesssim 5$ , where  $\tau_V$  is the radial optical depth through the midplane.

regions around intermediate-aged and evolved debris disks by future IR observational studies is one of the main motivations of the present paper.

There has been extensive work on disk modeling of both young optically thick disks and older optically thin disks. However, most of this work has concentrated on either solving the disk structure by setting the gas and dust temperatures to be equal (e.g. D'Alessio et al. 1998, 1999; Dullemond 2002; Dullemond, van Zadelhoff & Natta 2002; Lauchame, Malbet & Monin 2003), or has assumed a gas density and temperature distribution and solved for the chemistry (Willacy et al. 1998; Aikawa et al. 1999, 2002; Markwick et al. 2002; Ilgner et al. 2004). We solve for both the gas and dust temperatures and the chemistry simultaneously in our models, and use the gas temperature to calculate the vertical density profile. A similar theoretical study has been made by Kamp & van Zadelhoff (2001), where the authors attempted to explain the observed  $H_2$  emission from disks around two A stars, Vega and  $\beta$  Pictoris as seen by ISO and the lack of CO emission from these disks. These authors calculate the gas temperature by balancing the different heating and cooling mechanisms, but do not solve for the vertical structure of the disk. Our work adds the computation of vertical structure and is complementary to their model, since we focus on the *inner* regions of the disk, within about 20 AU from the star where the gas and dust are both warm ( $\sim 100$  K), whereas Kamp & van Zadelhoff (2001) considered disk regions from  $\sim 40 - 200$  AU. The inner regions are more interesting from the planet formation point of view, as many planets are expected to form close to the central star, within a few tens of AU if our solar system is typical. Furthermore, gas in regions far beyond this radius may be subject to photoevaporation from the central star and may be lost from the system early in its evolution. Our models are also complementary to the work of Glassgold, Najita & Igea (1997) and Glassgold, Najita & Igea (2004), who model the very innermost regions ( $r < 1$  AU) of young optically thick disks with emphasis on the problem of heating the surface layers and the near-infrared spectra.

The paper is organized as follows. In the next section, we briefly describe some of the physical processes we consider. In §3, we describe our model in detail. We present the results of a fiducial case (§4) and then in §5 present results where we vary most of the parameters to see how disk emission is affected by their values. This is followed by a discussion of our results and conclusions (§6).

## 2. Physical Processes in Disks

Our disk models include chemistry and thermal balance in a self-consistent manner and calculate the density and temperature structure of the disk in both the radial and vertical

directions. The vertical structure of the disk is calculated by balancing the hydrostatic thermal pressure gradient with the vertical component of gravity from the central star. The inner ( $r_i$ ) and outer ( $r_o$ ) boundaries of the disk and the distribution of the gas and dust surface density  $\Sigma(r)$  within these boundaries are input parameters. Our focus is on the IR emission detectable by the Spitzer Space Telescope, SOFIA or Herschel, and we therefore constrain our models to radial distances  $\sim 0.3 - 20$  AU from the central star, where gas temperatures range from  $\sim 1000$  K to 100 K respectively. The dust grains in this region are sufficiently warm to prevent ice formation on their surfaces, and therefore significant depletion of relatively volatile species such as gas phase O, C or S does not occur. We assume no significant opacity inside the inner edge at  $r_i$ , so that there is an “inner hole”.

Although we focus on intermediate-aged and older debris disks which are relatively optically thin in dust opacity, the gas opacity can in fact be quite large at line center of strong transitions and even for some FUV continuum bands, which lead to photodissociation and photoionization of abundant gas species. It is instructive to calculate a fiducial radial (hydrogen) gas column density  $N_H$  in the equatorial plane. Assuming a gas surface density distribution  $\Sigma(r) \propto r^{-3/2}$ , a vertical scale height of  $H = 0.1r$ , a gas mass of  $\sim 0.1$   $M_J$ , and an outer radius  $r_o = 20$  AU for a vertically isothermal disk, we find

$$N_H \approx 2.6 \times 10^{25} \left( \frac{1AU}{r_i} \right)^{3/2} \left( \frac{M_{gas}}{0.1M_J} \right) \text{ cm}^{-2}. \quad (1)$$

Since cross sections in the UV and X-ray for trace species can approach  $10^{-17}$   $\text{cm}^{-2}$  (or  $\lesssim 10^{-21}$  per H nucleus), we see that even small masses of gas can become optically thick in relevant bands. We also note that most of the opacity for radially declining surface densities is produced at  $r_i$ . If stellar photons make it through the shielding at  $r_i$ , they will generally penetrate the rest of the disk.

We emphasize that our disk model is hydrostatic and our thermal and chemical solutions are steady state. Therefore, we implicitly assume that the timescales to reach chemical/thermal steady state are short compared to dynamic timescales, i.e., the timescale for radial or vertical migration of gas. Because of the high densities and subsequent rapid cooling timescales, the assumption of thermal balance is well justified. Chemical timescales, however, can be quite long in cool ( $T \lesssim 300$  K) gas shielded from photodissociation. In such gas, cosmic ray ionization sets the equilibrium timescales to  $\sim 10^6$  years, which is comparable to radial drift timescales. However, this work represents an important first step in predicting the chemical and thermal structure of the warm  $T \sim 100 - 1000$  K,  $r \sim 1 - 20$  AU regions of evolved disks and predicting their spectrum.

We briefly describe below the chemical and physical processes considered in our models and refer the reader to the appendices for greater detail.

## 2.1. Dust Physics

Coagulation processes in intermediate-aged disks may lead to a distribution of solid particles which range in size from  $1 \mu\text{m}$  to  $10^4 \text{ km}$  (planets). We define “dust” to consist of all particles  $\leq a_{\max} = 1\text{mm}$  in radius. We assume that the size distribution of particles between  $a_{\min}$  and  $a_{\max}$  follows a power law  $n(a) \propto a^{-s}$ , where  $3 < s < 4$  such that most of the surface area is in the smallest particles and most of the mass is in the largest particles. Observational studies of disks estimate the “dust” mass from emission at wavelengths  $\simeq 0.4 – 2 \text{ mm}$ . If the size distribution has the above power-law form, these observational studies are only sensitive to the mass of dust in particles with sizes  $\lesssim 1 \text{ mm}$ .

Implicit in these assumptions is that most of the mass of solids will be “hidden” in large particles, rocks, boulders and planetesimals which emit insignificant amounts of infrared and millimeter wavelength radiation. Thus, at intermediate disk ages ( $\sim 10^7$  years), where dust has coagulated up to planetary sizes but where significant quantities of gas may not yet have been dispersed, the gas to “dust” (meaning  $a \lesssim 1\text{mm}$ ) mass ratio may increase above the value  $\sim 100$  characteristic of interstellar conditions. For example, if 90% of the mass of the primordial dust in a disk grows by runaway accretion to cores/embryos of sizes  $10^3$  to  $10^4 \text{ km}$ , and the remaining 10% of the mass is in solids with a distribution characterized by  $a_{\min} = 1\mu\text{m}$ ,  $a_{\max} = 100\text{km}$ , and  $s = 3.5$ , the gas to “dust” mass ratio increases to  $10^7$  without any gas or solid dispersion. Later, as the gas disperses, the gas to dust mass ratio may fall below the interstellar value.

In order to express the large range of gas to (small) dust mass ratios and the absolute values of the gas or dust mass which may exist as intermediate-aged or older disks evolve, we consider a range of gas masses  $M_{\text{gas}} \simeq 10^{-3} – 1 \text{ M}_J$  and a range of dust masses  $M_{\text{dust}} \simeq 10^{-7} – 10^{-4} \text{ M}_J$  (or  $f_D \sim 10^{-4} – 10^{-1}$ ).  $M_{\text{gas}}$  and  $M_{\text{dust}}$  are treated as independent variables, so that we cover gas-to-dust mass ratios of  $10^7$  to 10. We emphasize that these masses lie at  $r \lesssim 20 \text{ AU}$ . We do not consider gas masses smaller than  $10^{-3} \text{ M}_J$  because we find such small masses to be undetectable by the Spitzer Space Telescope, SOFIA or Herschel. We do not consider dust masses higher than  $10^{-4} \text{ M}_J$  because we find that the dust becomes significantly optically thick in the equatorial plane, and our model is valid only for small to moderate dust optical depths.

Our models consider gas and dust separately but as a coupled system, and they are capable of treating the dust grain density distribution independently of the gas density distribution as a function of radius  $r$  and vertical height  $z$ . In addition, the grain size distribution can be arbitrarily varied with  $r$  and  $z$ . However, for simplicity and to limit the number of models to be presented, we make the following assumptions.

1. We assume that the dust mass density distribution  $\rho_d(r, z)$  is proportional to the gas mass density distribution  $\rho(r, z)$ . That is, for a given disk we assume that the same gas-to-dust mass ratio applies everywhere in the disk. This assumption means that we ignore settling by grains to the midplane. Turbulence may stir the gas and dust sufficiently to justify this assumption (e.g. Balbus & Hawley 1991). However, our main motivation is simplicity in the models; presumably by using an average (vertical) mass ratio of gas to dust, we will obtain a first order solution for the more complicated case of vertical differentiation.
2. We assume that the grain size distribution does not vary with  $r$  or  $z$ . We consider our minimum grain size to be much larger than that in the interstellar medium. In intermediate-aged disks, the population of very small grains dwindles as coagulation processes lead to grain growth (e.g., Beckwith & Sargent 1996; Throop et al. 2001; Natta et al. 2004). In more evolved debris disks, small grains are continually replenished due to grinding down of larger objects by collisions, but radiation pressure forces act on sub-micron sized dust grains to rapidly remove them from the disk (Backman & Paresce 1993) on short timescales. Observations nevertheless seem to indicate the presence of small sub-micron sized particles (Li and Greenberg 1998) in a debris disk. We adopt a minimum grain size of  $a_{min} = 1\mu\text{m}$  for our standard case, but also consider other cases where we vary  $a_{min}$ . In this paper, we only consider  $n(a) \propto a^{-3.5}$ , i.e.,  $s = 3.5$ .

For a given mass in grains, the surface area  $\propto a_{min}^{-1/2}$ . Gas-grain collisional heating can be important in disks and due to their large surface area, small grains dominate the heating of the gas. Therefore, lowering  $a_{min}$  raises the gas-grain coupling and usually raises the gas temperature in the disk. Lowering  $a_{min}$  tends to raise the gas temperature for two other reasons. Smaller grains have higher efficiencies of heating the gas through the grain photoelectric heating mechanism (see Watson 1972; Weingartner & Draine 2001), which may dominate the heating once  $a_{min} \leq 10^{-2}\mu\text{m}$ . More importantly for this paper, smaller grains are hotter than larger grains due to the heating by stellar radiation and the inefficient radiative cooling of small grains. Grain absorption and emission efficiencies are dependent primarily on their physical size relative to the wavelength of emission or absorption, and their composition. For our models, we choose silicate (amorphous olivine) grains and the absorption coefficients are calculated from a Mie code (S.Wolf, private communication) based on optical constants from the Jena database (Henning et al. 1999). We divide the grain size distribution into 32 logarithmically spaced bins in size  $a$ , and each size grain has a different temperature at a fixed point in space.

We conclude this subsection with a discussion of the dust optical depths in the model

disks. Using the absorption coefficients discussed above, we calculate the optical depth  $\tau_V$  in the V band ( $0.5 \mu\text{m}$ ) of dust grains radially outward in the equatorial plane of the disk. For most of our models,  $\tau_V \lesssim 1$ . We do, however, run a few cases where the optical depth in the midplane  $\tau_V \sim 5$ . These disks are still optically “thin” in comparison to the younger, primordial dust disks where  $\tau_V \sim 10^3 - 10^4$ . In our calculation of dust temperatures we ignore the heating of dust grains due to the infrared radiation field emitted by the surrounding dust, but we include extinction of starlight by dust grains along the line of sight to a particular point in the disk. Even at optical depths  $\tau_V = 5$ , the dust grains are still primarily heated by attenuated starlight rather than by the re-radiated IR continuum field, so that our error in calculating the dust temperature is still small ( $\lesssim 10\%$ ), and our models are still valid. Typically, debris disks ( $t > 10^7$  years) have  $\tau_V \lesssim 10^{-2}$ . However, intermediate-aged disks ( $t \sim 10^{6.5}$  years) may have  $10^{-2} < \tau_V < 5$ .

## 2.2. Gas Chemistry

The chemical composition of the gas disk is critical to the structure and evolution of the disk. Although  $\text{H}_2$  cooling is often important in the radial range we consider, trace species such as S, O, CO and  $\text{H}_2\text{O}$  are often significant or even dominant coolants and for an accurate determination of the strength of emission lines, the abundances of atoms and molecules need to be calculated. Our treatment of disk chemistry is an adaptation of the Photodissociation Region (PDR) models of Tielens and Hollenbach (1985, hereafter TH85) and subsequent work (Kaufman et al. 1999). Elemental gas-phase abundances are taken from Savage & Sembach (1996) (Table 5, Appendix A). We use interstellar depletions of these elements, allowing for refractory dust but no ices in the  $r \leq 20\text{AU}$  disk region, where the dust is sufficiently warm to prevent ice formation. We have added sulfur chemistry and reactions of  $\text{CH}_3$  and  $\text{CH}_4$ , and there are a total of 73 species with atoms and ions of H, He, C, O, S, Fe, Mg, Si and molecules and molecular ions of H, C, O, S and Si (Table 6, Appendix A). To the PDR network of ion-neutral, neutral-neutral, and photoionization reactions, we have added X-ray photoreactions, and some high temperature reactions of importance under typical disk conditions. We have 537 reactions in all, with reaction rates in most cases taken from the UMIST Astrochemistry database (Le Teuff et al. 2000). A list of the added reactions, and the rates when they differ from the UMIST data, can be found in Table 7 (Appendix A).

The formation mechanism of  $\text{H}_2$  in disks may differ from the processes at work in the interstellar medium. In the ISM,  $\text{H}_2$  forms mainly on the surfaces of cold dust grains, with  $T_{dust} \lesssim 25 \text{ K}$ , typically. Dust in disks at  $0.3 - 20 \text{ AU}$  typically have temperatures  $T_{dust} \gtrsim 100 \text{ K}$ . It is not clear if H atoms would stick to such warm dust grains for sufficient time to allow

formation of  $\text{H}_2$  molecules (Hollenbach & Salpeter 1971; Cazaux & Tielens 2002). We have conservatively omitted grain formation of  $\text{H}_2$ . We find that other processes such as three-body reactions in dense regions and formation through  $\text{H}^-$  can completely convert atomic hydrogen to molecular hydrogen in self-shielded regions. We have also run cases including grain formation of  $\text{H}_2$  and find that the resultant infrared spectrum is not significantly altered.

Because the dust is optically thin, stellar and interstellar UV radiation is mainly attenuated in the disk by different gas species in various bands and lines. Large gas columns in the inner disk shield the outer regions from UV photodissociation caused by the central star. Similarly, the gas columns in the upper layers shield the midplane from the interstellar radiation field (ISRF). The self-shielding of  $\text{H}_2$  and CO, which involves absorption of specific resonance lines rather than continuum radiation, is treated analytically as in TH85. Attenuation of continuum FUV radiation by atoms and molecules is determined by splitting the FUV stellar radiation field into nine energy intervals, and the photon flux in each interval is calculated from the stellar (and ISRF) spectrum. The nine intervals from 0.74eV to 13.6eV include 0.74–2.6eV, 2.6–3.5eV, 3.5–4.3eV, 4.3–5.12eV, 5.12–7.5eV, 7.5–10.36eV, 10.36–11.26eV and 11.26–13.6eV where the lower and upper bounds in each case were chosen to correspond to dominant photoabsorption thresholds of species in each energy bin. The attenuated photon flux in each bin at a given position in the disk is dependent on the column densities of all the absorbing species towards the line-of-sight to the source. Photodissociation and photoionization reaction rates are thus accurately computed by taking into account the attenuation of photons in the energy range where absorption cross-sections peak.

We also consider the effects of X-ray radiation from the star on the disk. X-ray luminosities of  $\sim 10^{-4} \text{ L}_{bol}$  have been observed in stars as old as  $10^7 - 10^8$  years, and therefore include not only intermediate-aged disks but also a number of observed “debris disks”. X-rays affect the chemical structure of the disk through ionizations and heat the gas via collisions with secondary electrons generated by the X-ray produced primary electron. X-ray heating and chemistry may dominate in the inner regions of the disk and the surface layers where attenuation by gas is low. Stellar X-ray spectra from weak-line T Tauri stars peak at about 1–2 keV (e.g., Feigelson and Montmerle 1999) and the flux drops rapidly as the X-ray photon energy increases. Soft X-rays, with energies  $\lesssim 1$  keV, do not penetrate significantly through a massive disk, their typical attenuation columns being about  $10^{21-22} \text{ cm}^{-2}$  of gas. The penetration columns are larger by about two orders of magnitude for harder (3–10 keV) X-rays, but the stellar flux and photoabsorption cross-sections decrease sharply to make their influence on disk chemistry relatively unimportant in the shielded regions of the disk. On the other hand, in disks with low masses or lower column densities towards the line of

sight to the star (disks with large inner radii, for example), X-rays incident on the disk heat, ionize and dissociate significant numbers of atoms and molecules in the gas and our chemical code treats this chemistry in detail. For simplicity, we do not consider double or higher ionizations, as in Maloney et al. (1996). The total X-ray photoabsorption cross section of the gas is taken from Wilms, Allen & McCray (2001), adapted to our gas-phase abundances (see Appendix B). We use the photoionization cross sections as originally published by Verner et al. (1993) and later updated by Verner & Yakovlev (1995). The primary ionization rates for each species are calculated for each species by integrating the product of the attenuated photon flux and the absorption cross section over the X-ray energy range (Maloney et al. 1996). We also include secondary ionization rates and X-ray induced FUV radiation and the resulting photochemistry (Maloney et al. 1996). The details of our treatment of X-ray chemistry and heating are given in Appendix B.

### 2.3. Heating and Cooling Processes

One of the major innovations of this paper in terms of disk modeling is the separate calculation of gas and dust temperatures. Most previous models (with the exception of Kamp & van Zadelhoff 2001) assume that the gas temperature equals the dust temperature. While this is certainly true in the midplanes or central regions of very optically thick disks, it is not as true for debris disks, intermediate-aged disks, or the upper regions of younger, optically thick disks. Here, the relatively weak thermal coupling between gas and dust, and the different processes which heat and cool the gas and dust, can lead to significant temperature differences. This point was also made by Chiang & Goldreich (1997), who note that the gas temperature in the superheated layers of passive, optically thick dust disks can be significantly lower than the dust temperature due to molecular cooling.

Gas in disks can be heated through many different mechanisms, and we consider the physical and chemical processes that are likely to dominate in these environments. The heating of dust grains by the stellar radiation field and subsequent collisions with gas molecules transfers kinetic energy to the gas thereby heating it. Gas-dust collisions are the dominant heating mechanism for the gas through most of the disk, except in regions where the gas is heated to temperatures higher than the dust by other processes and here collisions with dust cool the gas. In regions where the columns through the disk are small enough to allow the penetration of FUV radiation, and  $H_2$  is photodissociated to form atomic hydrogen, the heat associated with the formation of  $H_2$  raises the temperature of the gas. X-rays from the central star directly heat the gas and dominate the gas heating at the surface and in the inner disk. In addition to these mechanisms, we also include heating due to collisional

de-excitation of vibrationally-excited  $H_2$  molecules, grain photoelectric heating, drift heating due to dust, exothermic chemical processes, photoionization of neutral carbon, and cosmic rays. All the heating mechanisms considered are described in some detail in Appendix C.

The gas in the disk is mainly cooled through radiative transitions of the different species and, where the gas is warmer than the dust, through gas-grain collisions. We include cooling due to the fine structure and metastable lines of CI, CII, OI, OII, FeI, FeII, Si, SII, SiI, SiII, the rotational lines of  $H_2$ ,  $H_2O$ , OH, CO, CH,  $HCO^+$ , and by Lyman  $\alpha$ . We also include cooling due to the collisional ionization of atomic species, and vibrational cooling due to  $H_2$ . Vibrational cooling due to CO was found to be unimportant for the disk parameters considered in this paper. For all the molecular rotational levels, except for  $H_2$  and CO, we use the analytical formulae of Hollenbach & McKee (1979, hereafter HM79). We derive new fits to their formulae for  $H_2O$  (ortho and para states) and OH (see Appendix D) using collisional rate data for 167 and 45 levels respectively. It was computationally expensive to include a detailed multi-level calculation for these molecules in the code, and we estimate the strengths of individual  $H_2O$  and OH lines using the derived density and temperature structure and solve for the level populations after a disk solution for the temperature, density and chemical abundance structure (i.e., the  $r, z$  dependence) has been obtained with the new analytical approximations for the total cooling by OH and  $H_2O$  molecules. We note that cooling transitions are often optically thick, and we use the escape probability formalism described in HM79.

We solve for the rotational cooling due to  $H_2$  in detail because one of our primary aims is to calculate the strength of the  $H_2$  emission lines from the disk. We include the first 20 levels of molecular hydrogen in our calculation of the cooling, and derive the population of each individually excited level. We have also added vibrational cooling of  $H_2$  as in HM79 and cooling due to collisional dissociation of  $H_2$  molecules. We do a similar calculation of the first 20 rotational levels of CO and solve for the level populations to compute the total CO cooling.

### 3. Disk Model

In this section, we describe our disk model, discuss some of our assumptions and give the details of our numerical scheme for obtaining a disk solution. Because our main aim is to characterize observed emission from disks and infer disk properties from the comparison of observed spectra with our models, we have varied most of our input parameters across a wide range. However, we define a “standard case” where we assign typical values to each parameter. The results from the standard model are described in §4.

**Surface density distribution** We assume a power law distribution of surface density of both gas and dust with radius,  $\Sigma(r) \propto r^{-\alpha}$ , where  $r$  is the distance from the star. The nominal value for  $\alpha$  is often taken to be 3/2 in the literature (Lynden-Bell & Pringle 1974; Chiang & Goldreich 1997). For our standard case, we assume a flatter surface density distribution defined by  $\alpha = 1$ , motivated by observations of disks (Dutrey et al. 1996, Li & Greenberg 1998). The main effect of changing the slope of the surface density distribution is to alter the relative distribution of mass in the inner and outer disk. This changes both the slope of the dust continuum emission at longer wavelengths and the relative strengths of the gas emission lines that preferentially originate either in the warmer inner disk or the colder outer disk region. We study the effects of a change in the surface density distribution by varying  $\alpha$ . As long as  $\alpha < 2$ , most of the disk mass is in the outer regions; and for  $\alpha > 0$  (and assuming a vertical scale height  $H$  that increases with  $r$ ), most of the radial opacity occurs in the inner regions.

**Radial extent** Our model disk is defined to have both an inner and outer edge. It is not, however, certain whether an inner (gas) hole would exist in evolved disks, even if the dust is heavily depleted in the inner regions. Theoretical models of dust disks often assume an inner truncation radius determined by the dust sublimation temperature, interior to which there is no dust (e.g., Bell et al. 1997; Chiang & Goldreich 1997; D’Alessio et al. 1998; Dullemond et al. 2002). SED modeling of observed dust disk emission also argues for the presence of inner (dust) holes in many disk systems (e.g., Natta et al. 2001, Dullemond et al. 2001). In evolved disks, where planetary formation is likely to have taken place, an inner gas cavity may be generated by massive planets that prevent outer gas from accreting onto the star, whereas viscous accretion of gas interior to the massive planets may rapidly drain gas there.

The inner disk radius  $r_i$  is an important parameter of our models because it determines the penetration of stellar radiation into the disk and contains the hottest gas and dust. Emission from this region, therefore, is a dominant contributor to the higher frequency continuum from the dust and the higher excitation lines of the gas. Small values of  $r_i$  imply higher densities and column densities at the inner edge and radiation can penetrate only a short distance into the disk before being attenuated. If disks with the same gas mass have larger  $r_i$ , there is less rapid attenuation of stellar photons. Consequently, photodissociation and photoionization by X-rays and FUV radiation extends further into the disk and affects more of the gas mass. Observations of intermediate-aged and debris disks indicate disk inner radii ranging from a few tenths of an AU to tens of AUs (e.g., Liu et al. 2004, Calvet et al. 2002, Li & Greenberg 1998). For our standard case we assume an inner radius of  $r_i = 1$  AU. However, we include several cases where we vary the inner radius to see how this parameter affects disk thermal structure and chemistry and the resultant spectrum.

We also define an outer disk radius  $r_o$ . Our fiducial disk is truncated at  $r_o = 20$  AU. Unlike  $r_i$ , the exact choice of  $r_o$  does not affect our results significantly because any gas beyond  $r_o$  will be too cold to significantly contribute to the IR lines we focus on in this study. The choice of 20 AU is motivated by the following four reasons. (i) Disks may lose much of the outer gas through the process of photoevaporation early in their evolution (Hollenbach et al. 1994; Adams et al. 2004). (ii) Our interest lies in the planet-forming regions of the disk, and from our understanding of the formation of the solar system and of the evolution of disks, planet formation appears to take place within a few tens of AU from a star. (iii) Glassgold et al. (2004) present models of inner ( $< 1$  AU) disks whereas Kamp & van Zadelhoff (2001) present models of outer ( $\geq 30$  AU) disks. We, therefore, present this complementary study, which is especially relevant to the Spitzer Space Telescope, SOFIA and Herschel since the gas and dust temperatures span a range ( $\sim 50$  K - 500 K) which produce copious IR emission in the  $4 \mu\text{m} - 200 \mu\text{m}$  wavelength range. Mid-infrared emission from gas species at temperatures less than  $\sim 100$  K is likely to be insignificant, so the neglect of any gas beyond  $r_o$  does not affect our emission line calculations. (iv) Gas molecules, such as  $\text{H}_2\text{O}$ , may freeze on grain surfaces when the dust grain temperature drops below  $\sim 80 - 100$  K. We therefore truncate the disk at a radius where ice mantle formation is likely to become important on grains, i.e., when dust grain temperatures fall below  $\sim 100$  K. To summarize points (iii) and (iv), the outer edge need not correspond to a real cut-off in surface density. We are interested in the IR emission from warm gas in the  $r \lesssim 20$  AU region. Material beyond this outer radius will be either too cold or frozen on grain surfaces to radiate appreciably as IR line emission from gaseous species.

**Stellar Spectrum** The stellar spectrum is chosen to be a modified Kurucz model, and we consider stars of two spectral types, a G star at 6000 K and a cooler K star with a temperature of 4000 K. The central star at these disk ages is expected to have a significantly higher FUV luminosity than its main-sequence counterpart and we account for this increased luminosity in our stellar models. An accurate determination of the FUV flux is especially important in solving for the disk chemistry as the FUV initiates numerous photodissociation and photoionization reactions. We follow a prescription by Kamp & Sammar (2003) for our age-dependent FUV fluxes, where the FUV flux scales inversely with the age of the star (Ayres 1997). We assume an age of  $10^7$  years for the G star in our models. IUE and rocket experiment data are added to a Kurucz photosphere model to thus obtain a semi-empirical age-dependent spectrum for a G2 spectral type star. We use chromospheric models by Cohen(private communication) for the star  $\epsilon$  Eri as our input stellar model for the K star. Figure 1 shows the spectra we use, the solid line indicates the G star and the dashed line the K star.

For the stellar X-ray spectrum, we use a broken power-law fit to ROSAT observations (Feigelson & Montmerle 1999) for a wTTs, where the luminosity per keV peaks at about 2 keV. The luminosity per keV is thus given by  $L(E) \propto E^{-1.75}$ ,  $E \geq 2$  keV and  $L(E) \propto E$  for  $E < 2$  keV. This X-ray spectrum is normalized to the stellar X-ray luminosity between 0.5–10 keV. For our fiducial case, the X-ray luminosity is assumed to be  $10^{-4}$  times the bolometric luminosity of the star.

**Numerical model** The disk density and temperature structure is calculated iteratively from the midplane to the surface starting at  $r = r_i$  and then working radially outward in the disk. We start with an estimate of the gas density at the point ( $r = r_i, z = 0$ ) and compute the dust and gas temperatures.

The dust temperature is calculated from thermal balance between the absorption of stellar radiation by the dust and subsequent re-emission in the infrared. Heating of a grain due to absorption of infrared radiation coming from surrounding dust particles is ignored in our optically thin dust disk models. The dust temperature (at a given size  $a$ ) needs to be iterated only because the dust vertical distribution is determined by the gas vertical distribution, and the dust temperature is a function of  $z$  because of the varying distance to the star.

The gas temperature is determined by thermal balance between the heating and cooling processes described earlier, and this then determines the gas pressure. The condition of vertical hydrostatic pressure equilibrium,

$$\frac{dP}{dz} = \frac{-GM_*\mu m_H n_H(r, z)}{(r^2 + z^2)^{3/2}} \quad (2)$$

determines the pressure as a function of disk height, where  $P = k_B(n(\text{H}) + n(\text{H}_2) + n(\text{He}))T_{\text{gas}}$ ,  $\mu$  is the mean molecular weight,  $m_H$  is the mass of a hydrogen atom,  $n_H$  is the hydrogen nucleus number density, and  $n(\text{H})$ ,  $n(\text{H}_2)$  and  $n(\text{He})$  are the number densities of atomic and molecular hydrogen and helium respectively. At each height  $z$  from the midplane, the density and temperature combination that gives the pressure from Eq.(2) is found. The vertical grid is adaptive in nature and determined by the condition of pressure gradient balancing gravity. The vertical increments in height are chosen to correspond to equal factors of decrease in thermal pressure (a factor of 0.8 in most cases) and for regions where the temperature slowly varies with  $z$ , this also corresponds to a logarithmically decreasing column density in each cell. This ensures that the escape probabilities for the cooling transitions increase slowly and smoothly as we get farther from the midplane, and enables accurate determination of the gas temperature. We ensure that the density contrast from surface to midplane is at least four orders of magnitude, and the number of cells and their spacing are calculated to meet all

these criteria. After the entire vertical grid has been solved, the gas density is integrated over  $z$  and compared to the required gas surface density,  $\Sigma(r)$ . The midplane density is re-scaled and the vertical temperature and density structure is thus iterated until the surface density converges to the required value.

Once we have the solution at  $r_i$ , we move outward to solve at the next radial grid point. The radial grid is logarithmically divided in  $r$ , except for the inner disk which is more finely sub-divided. The column density towards the star is dominated by the dense inner regions, and this is where the gas absorbs most of the stellar FUV and X-rays. This attenuation needs to be calculated accurately, and we have divided the inner disk into cells of slowly increasing column density going outwards in  $r$ , with the first radial cell (at midplane) having a hydrogen gas column density  $10^{20} \text{ cm}^{-2}$ , which corresponds to a small attenuation of the X-ray and UV fluxes.

#### 4. Standard Disk Model Results

In this section, we describe in some detail the results of our fiducial disk model (“the standard case”), the input parameters for which are listed in Table 1. The standard model has a gas mass  $M_{\text{gas}} = 10^{-2} \text{ M}_J$  and dust mass  $10^{-5} \text{ M}_J$ . In the next section we present a full parameter study varying both the gas mass and the dust mass, the main parameters of this work. The other parameters we treat as “minor” parameters, and in the next section we vary each of these parameters in turn, holding all other parameters at the fiducial values, and study its effect on disk structure and emission. These minor parameters include the disk inner radius, the minimum grain size, the stellar X-ray flux and the surface density distribution.

Our fiducial gas to dust mass ratio of  $10^3$  is higher than the interstellar value, but, as we have discussed, this is possible at an intermediate stage where dust has coagulated but gas has not yet dispersed. We have chosen this value for our fiducial case primarily because, as shall be shown below, this ratio allows detection of gas emission lines over the continuum for the smallest gas masses with the dust midplane optical depth still being  $\lesssim 1$ .

Our standard model disk solution results in a flared disk with an inner puffed region where the gas is subject to the unattenuated, strong stellar radiation field and heated to high temperatures. Dullemond et al. (2002) find a similar effect in younger, optically thick (in dust) disks. Figure 2 shows the disk surface where the density is  $10^{-4}$  times the density in the midplane and contours where the vertical column densities to the surface are  $10^{21}$  and  $10^{22} \text{ cm}^{-2}$ . Stellar UV and X-ray fluxes are absorbed at these column densities, and hence

in these regions. The hot inner edge or rim has a somewhat lower density compared to gas just beyond the edge because it is hotter and more extended vertically. This region shields much of the rest of the disk from UV and X-ray photodissociation and photoionization by starlight. The density increases slightly with radius progressing from this inner edge as the temperature falls steeply, and the disk scale height decreases. Recall that for a vertically isothermal disk the scale height  $H$  of the disk is given by  $H \propto (r^3 T(r))^{1/2}$  (e.g., Adams, Shu & Lada 1988, Shakura & Sunyaev 1973). Therefore for a radial temperature gradient steeper than  $1/r^3$ , the scale height decreases with radius. Further into the disk, the temperature falls less steeply and here  $H/r$  now increases with radius, giving rise to a flared disk solution. The density falls less steeply with height as compared to an vertically isothermal solution in most regions of the disk, because the gas temperature in general rises with  $z$ . We first describe the main heating and cooling mechanisms in the disk and the resulting temperature structure and then discuss the chemistry and emission from the disk.

#### 4.1. Heating, Cooling and Temperature Structure

Figures 3, 4, 5 and 6 show the heating, cooling and the radial temperature and density structure in the disk at the midplane and the vertical temperature and density structure in the disk at two typical radii, of 2 and 10 AU. Figure 3 shows the main heating terms for our standard case in the midplane of the disk, as a function of disk radius. Heating due to formation of  $H_2$  is high where hydrogen is predominantly atomic, but quickly decreases as self-shielding turns the gas molecular, at hydrogen nuclei column densities of  $\sim 10^{21-22} \text{ cm}^{-2}$ . X-rays are a strong heating agent in the unshielded innermost regions of the disk, but get attenuated rapidly due to the high midplane radial column density  $N(r) \sim 10^{24} \text{ cm}^{-2}$  (see Eq.(1)). The penetration column for 2 keV X-ray photons, where the X-ray spectrum peaks, is  $\sim 1/\sigma(E) \sim 5 \times 10^{22} \text{ cm}^{-2}$  which implies a penetration depth of  $\sim 0.003 \text{ AU}$ . Heating due to X-rays becomes unimportant in the midplane for  $r \gg r_i$  into the disk. X-rays, however, can penetrate further at the surface of the disk, where the attenuation columns of gas towards the line-of-sight to the star are low. X-rays are the dominant heating mechanism at the surface. Gas-grain collisions are the strongest gas heating source through most of the equatorial regions of the disk even though the dust surface area per H nucleus is much smaller than the interstellar value ( $\sim 10^{-3}$  times that in the ISM for the standard case). Note that in the innermost regions, the gas-grain collisions become a cooling mechanism, rather than a heating mechanism, as the gas becomes hotter than the dust grains due to X-ray and  $H_2$  formation heating. Heating due to cosmic rays, grain photoelectric heating and drift heating are negligible in this disk model. Kamp & van Zadelhoff(2001) find drift heating to be the dominant heating agent in their models of gas disks around A stars, but

we find that our more careful calculation of drift velocities yields values that are typically too low ( $\sim 10^3$  cm s $^{-1}$  or less) for viscous heating to be important in our  $\sim 20$  AU disks. Nevertheless, we include this mechanism as it may become important in other regions of parameter space. The dominant coolants in the midplane of the disk (Figure 4) are OH, H<sub>2</sub>O, SI, SiII, H<sub>2</sub> and FeII in the inner regions and OI, CO and OH in the outer disk. Above the midplane SI and OI are strong coolants. At radii larger than  $\sim 7$  AU, the IR continuum field from the warmer dust excites the upper level of the [SI] line, and subsequent collisional de-excitation leads to a gas heating rather than cooling by this line, as seen by the sharp cutoff in the SI cooling in figure 4.

The gas temperature in the midplane of the disk (Figure 5) decreases with radius approximately as  $T_{gas} \propto r^{-0.8}$ . The plot also shows the dust temperatures of the smallest and largest grains. These temperatures are higher than that of the gas over most of the disk interior and therefore gas-grain collisions heat the gas here. In the outer regions of the disk midplane, the gas temperature falls well below the dust temperature, as the decreasing density leads to a decrease in collisional coupling between grains and dust which lowers the heating rate of the gas. Figure 5 also shows the number density of gas in the midplane which falls approximately as  $1/r^2$ .

Figure 6 shows the variation of gas temperature with height at two different disk radii, 2 and 10 AU, and the gas number density with height at 2 AU, with the dominant heating sources and coolants marked at various heights. In the equatorial region where gas-grain collisions dominate the heating, the density (dashed line in Figure 6) can be seen to decrease rapidly with  $z$  (recall that for isothermal disks,  $n \propto e^{-z^2/H^2}$ , where  $H$  is the scale height), leading to a reduced gas-grain coupling and heating, and causing a drop in temperature with height. Several scale heights above the midplane, the attenuating column to the star drops to sufficiently low values that X-ray heating begins to dominate and the gas temperature rapidly rises. The main coolant at the surface is [OI]63 $\mu$ m, which is optically thick at these column densities. The column to the surface decreases with height, and the line becomes more optically thin and more efficient at cooling. This leads to a drop in temperature again in the upper disk atmosphere. Figure 6 also shows the temperature profile at a larger disk radius (10AU), where gas temperatures are much lower. The main heating sources remain gas-grain collisions at the midplane and X-rays at the disk surface, but the main coolants in these regions are CO and OI, as the temperatures are too low ( $< 100$  K) to significantly excite the transitions of H<sub>2</sub>, SI, SiII or FeII, and the densities and OH and H<sub>2</sub>O abundances are too low for OH and H<sub>2</sub>O to dominate the cooling.

**Chemistry** Figure 7 shows the abundances of various species as a function of height above the disk at a radius of 2 AU. We discuss below the essential species in the hydrogen, OH/H<sub>2</sub>O, C<sup>+</sup>/C/CO, Si<sup>+</sup>/Si, Fe<sup>+</sup>/Fe, and S<sup>+</sup>/S chemistry.

In the innermost disk, for  $r \lesssim 1.1$  AU, hydrogen is predominantly atomic. H<sub>2</sub> is formed via reactions of H with H<sup>+</sup> and three body reactions, but is rapidly destroyed by reactions with O to form OH and by photodissociation. In regions high above the midplane, where there is less attenuation of stellar UV, photodissociation of H<sub>2</sub> dominates. Beyond 1.1 AU, self-shielding prevents UV photodissociation of H<sub>2</sub>. The destruction reaction with O has a high activation barrier at  $\Delta E/k = 3200$  K and this reaction rate rapidly falls as the temperature decreases radially outward. Consequently, hydrogen turns fully molecular in the dense midplane at  $r \sim 2$  AU. At the surface of the disk at  $r = 2$  AU, lower attenuation columns lead to photodissociation of H<sub>2</sub>, and hydrogen is atomic as is shown in Figure 7.

Carbon turns molecular in the midplane even at the inner edge of the disk where hydrogen is still atomic, and is in the form of CO throughout the disk midplane. In the upper regions of the disk, CO is photodissociated into atomic carbon, which gets ionized even higher up in the disk to form C<sup>+</sup> (Figure 7). CO is formed via the reaction of C with OH in the inner disk where the temperatures are high and OH is more abundant. O reacts with CH to form CO in the outer disk. The main destruction routes of CO are photodissociation by the stellar UV field at the inner edge of the disk and in regions above the midplane everywhere in the disk. In the shielded interior of most of the disk, all the available carbon forms CO, as the only destruction mechanism for CO molecules is collisions with the very few He<sup>+</sup> ions that are formed by cosmic rays.

The gas phase elemental oxygen abundance is a factor of 2.3 higher than the carbon abundance (Table 5, Appendix A) and all the oxygen not locked up in CO is in the form of OI throughout the disk. The stellar photons are not energetic enough to ionize oxygen, and trace amounts of the atomic oxygen form O<sub>2</sub>, OH and H<sub>2</sub>O. In the inner disk, where the temperature is high ( $T > 300$  K), O reacts with H<sub>2</sub> to form OH, which then reacts again with H<sub>2</sub> to form water. OH also reacts with O to form O<sub>2</sub> throughout the disk, which is destroyed by photodissociation. H<sub>2</sub>O and OH are the dominant coolants at the high densities and temperatures in the innermost disk. Water is photodissociated through the disk more readily than OH as it has a lower photodissociation threshold ( $\sim 4.3$  eV). In disks that are more massive, larger attenuation columns shield H<sub>2</sub>O from photodissociation and due to its high abundance it dominates the cooling, as will be discussed later. As the temperature drops further into the disk, the production of OH and H<sub>2</sub>O drops, because the reactions of O and OH with H<sub>2</sub> have high activation barriers. The resulting decrease in the abundance of OH lowers its strength as a coolant further into the disk. The destruction of OH is

mainly via photodissociation which rapidly decreases with disk radius as the optical depth in the relevant FUV band increases, and this keeps the abundance of OH from dropping sharply. The main reaction for the production of OH and H<sub>2</sub>O in the cooler outer regions is recombination of H<sub>3</sub>O<sup>+</sup>, which is initiated by cosmic ray ionization of H<sub>2</sub>.

Sulfur is predominantly atomic throughout most of the disk, except very near the midplane where it is partly molecular and at the disk surface where it is ionized to form SII. In more massive disks, which shield sulfur molecules from photodissociation, we find that most of the sulfur is SO<sub>2</sub> at regions near the midplane. Silicon and iron are ionized through most of the disk, and are neutral only in denser disks where there is sufficient shielding from photoionization. Limited silicon chemistry is included in our models and we find that silicon is ionized through most of the disk. For more massive disks with  $M_{gas} > 0.1 M_J$ , silicon is atomic in dense regions such as near the midplane, but does not turn molecular even for our most massive disks.

SI, SiII, FeII and H<sub>2</sub> S(0) all have their first excitation level  $\sim$ 500 K above ground and are excited under similar conditions. The gas needs to be warm,  $\gtrsim 100$  K for emission from these lines to be strong. Note that sulfur is a much stronger coolant than H<sub>2</sub> though both species have similar excitation energies. At disk gas densities, these coolants are in LTE so that their cooling is proportional to their abundance times their spontaneous transition probability. Though the abundance of sulfur is 4.5 orders of magnitude lower than that of H<sub>2</sub>, its spontaneous transition probability is  $4.7 \times 10^7$  that of H<sub>2</sub> S(0). Thus, at high densities, and assuming the lines are optically thin, [SI]25.23 $\mu$ m should dominate H<sub>2</sub> 28  $\mu$ m by a factor  $\sim$ 1000. In fact, the [SI]25 $\mu$ m transition is optically thick, so that the [SI]25 $\mu$ m line is typically  $\sim$ 10 times the H<sub>2</sub> line strengths. Cooling from SI decreases as the gas temperature decreases, and in the outer disk the most important coolants are CO and OI at the midplane and OI at the surface where CO is photodissociated.

**Disk emission and spectrum** Figure 8 shows a model spectrum for this standard disk at a distance of 30 pc, with the dominant lines in the 5–40  $\mu$ m band, superimposed on the dust continuum. (The resolution of Spitzer-IRS in the high-resolution mode ( $R = 600$ ) has been assumed for computing the emission spectra.) The lines shown in the emission spectrum are strong enough for nearby sources ( $\lesssim 100$  pc) to be potentially observable by the Spitzer Space Telescope, or future infrared telescopes, such as SOFIA or Herschel. The IRS instrument on the Spitzer Space Telescope has a  $3\sigma$  flux detection limit of  $\sim$ 10<sup>−18</sup> W m<sup>−2</sup>, with an integration time of  $\sim$ 500s.

The [SI]25.23 $\mu$ m line stands out as a strong coolant in our disk spectrum and as an important diagnostic of the presence of gas at  $\sim$ 1 AU in disks. The possible detection of gas

disks in sulfur is one of our main results, as in many cases this line dominates the spectrum and is stronger than the  $H_2$  lines. The  $[OI]63\mu m$  and  $[SI]56.0\mu m$  lines may also be strong enough for detection by SOFIA. Other detectable lines in this figure are the  $H_2$  S(1) and S(2) lines, the  $[FeII]26.0\mu m$  line, the  $[SiII]34.8\mu m$  line, and water lines at  $33\mu m$  (o- $H_2O$ ,  $6_{6,1} \rightarrow 5_{5,0}$ ) and  $36\mu m$  (o- $H_2O$ ,  $6_{5,2} \rightarrow 5_{4,1}$ ).

Figure 9 shows a similar spectrum for a disk with an inner radius of 10 AU, which is seen to have no strong OH or  $H_2O$  lines, but has detectable  $H_2$  S(1),  $H_2$  S(2),  $[SI]25.23\mu m$ ,  $[FeII]26\mu m$  and  $[SiII]34.8\mu m$  lines. The effect on the gas of changing the inner disk radius is discussed in more detail in §5.2.

Table 2 lists the observable mid-infrared and far infrared lines with their wavelengths and the telescope instruments that can observe them. Gas emission lines are potentially important diagnostic tools of physical and chemical conditions of gas in disks and could be useful in detecting even very small amounts of gas. However, most of these lines are optically thick with the exception of  $H_2$  S(0) and would correspondingly diminish in strength with the inclination of the disk, being the strongest for a face-on orientation. Molecular hydrogen remains optically thin in the S(0)  $28\mu m$  line and the line strength is not affected by the orientation angle of the disk. Moreover, it is less dependent on the chemical network and the cosmic abundances assumed and directly traces the gas in the disk. However, the  $H_2$  S(0) line is weaker than other gas emission lines and hence is more difficult to detect. For pure sensitivity to the presence of small amounts of gas at  $r \sim 1 - 2$  AU, the  $[SI]25.23\mu m$  line is predicted to be the best probe.

## 5. Parameter Survey and Emission Line Detectability

### 5.1. Variation of Spectra with $M_{gas}$ and $M_{dust}$ .

We have conducted a parameter survey to explore the probability of gas emission line detection above the dust continuum emission for a range of gas masses and dust masses and for a range of stellar and disk parameters (Table 3). We limit the range of parameters to those which might give us detectable infrared line fluxes, and those whose dust optical depths  $\tau_V \lesssim 5$ . Figure 10 shows the change in IR line luminosities due to variations in gas and dust masses. For a disk at a distance of 30 pc, the flux detection limit of the IRS (high resolution) instrument on Spitzer for a  $3\sigma$  500-second detection corresponds to a line luminosity of  $\sim 3 \times 10^{-8} L_\odot$  (or  $10^{-18} W m^{-2}$ ). For comparison, SOFIA at these wavelengths (10-28  $\mu m$ ) has a minimum detectable  $3\sigma$  line flux of  $\sim 10^{-17} W m^{-2}$  ( $3 \times 10^{-7} L_\odot$ ), and Herschel  $\sim 7 \times 10^{-18} W m^{-2}$  ( $2 \times 10^{-7} L_\odot$ ) at its shortest observing wavelengths (60-200

$\mu\text{m}$ ). Instruments on both telescopes have resolving powers  $\sim 10^{3-4}$ . Figure 11 presents these results in an alternate way, which readily shows the parameter space where lines are detectable.

The S(1) and S(2) lines of  $\text{H}_2$  arise from gas with temperatures  $\gtrsim 150\text{-}200\text{ K}$ , whereas S(0) emission has a significant contribution from slightly cooler gas ( $T \gtrsim 100\text{ K}$ ). At very low gas masses ( $10^{-3} \text{ M}_J$ ), the midplane column density through the disk is  $\sim 10^{23} \text{ cm}^{-2}$ , and hence low enough to allow penetration by stellar UV and X-ray photons through much of the inner disk and to photodissociate  $\text{H}_2$ . The low amount of warm  $\text{H}_2$  gas results in very low line strengths of all three  $\text{H}_2$  lines, as can be seen in Figure 10. As the disk gas mass is increased to  $10^{-2} \text{ M}_J$ , the column density increases allowing shielding of  $\text{H}_2$ , increasing its abundance in the inner, warm regions of the disk. The gas in the inner disk where the emission from the S(1) and S(2) lines peak, is heated by collisions with dust,  $\text{H}_2$  formation heating and by X-rays. The increased amounts of warm  $\text{H}_2$  gas ( $\gtrsim 100\text{ K}$ ) result in a sharp increase in the line strengths. As the gas mass is further increased to  $0.1 \text{ M}_J$ , the gas temperature at a fixed radial column density initially decreases because the  $\text{H}_2\text{O}$  cooling rises faster than the X-ray heating with density. Thus, there is less mass and surface area of warm gas. As the gas mass increases to  $\sim 1 \text{ M}_J$ , the gas heating by gas-dust collisions takes over and raises the gas temperature and the S(1) and S(2) luminosities. The S(0) line emission peaks at regions slightly further out where dust dominates the heating and it monotonically increases with gas mass. At low gas masses, the observed  $\text{H}_2$  S(0) emission directly correlates with the mass of *warm* gas in the disk, regardless of the dust or total gas masses, and the warm gas ( $T \gtrsim 100\text{ K}$ ) mass in a disk at 30 pc needs to be above  $\sim 10^{-3} \text{ M}_J$  for detection by the Spitzer Space Telescope. At higher gas masses,  $\sim 1 \text{ M}_J$ , dust collisions are the main heating mechanism that heat  $\text{H}_2$  gas. In these relatively massive disks,  $\text{H}_2$  line emission does not increase proportionately with mass, as the lines start to become optically thick (at disk gas masses  $\gtrsim 0.05 \text{ M}_J$  for S(1) and S(2),  $\gtrsim 0.2 \text{ M}_J$  for S(0)). Figure 10 shows that for line luminosities  $\gtrsim 5 \times 10^{-8} \text{ L}_\odot$ , the luminosity generally scales with a low power ( $< 1$ ) of gas mass. This means that for disks at distances  $d \gg 30$  pc, considerably more gas mass is required for detection than if  $L \propto M_{\text{gas}}$  is assumed. This important point will be discussed more in §6.

An increase in total dust mass of the disk produces increased emission due to an increase in heating of the gas via gas-dust collisions. Dust collisions are an important heating mechanism in the bulk of the  $\text{H}_2$  emitting regions. As the dust mass is decreased, the decreased coupling between gas and dust lowers the gas heating rate and the gas temperature and therefore the emission. On the other hand, dust produces IR continuum emission which can obscure the detection of infrared lines (typically, systematics introduce baseline variations which make it impossible to detect lines at the  $\lesssim$  few per cent continuum level). There is

thus an optimal gas-to-dust mass ratio  $\sim 10^3 - 10^5$  and gas mass  $\gtrsim 10^{-2} M_J$  (for disks at 30 pc) where  $H_2$  emission can be detected. Given  $\gtrsim 10^{-2} M_J$  of total gas mass, a gas to dust mass ratio  $\lesssim 100$  produces a line to continuum ratio of  $\lesssim 5\%$  for the highest Spitzer Space Telescope resolving power ( $R=600$ ), rendering the line difficult to detect above the strong continuum. On the other hand, if the dust abundance is lowered to the point where the gas to dust ratio  $\gtrsim 10^5$ , then the grain-gas collisional heating is so drastically reduced that the gas is cold, and the  $H_2$  lines are too weak to detect in the absence of other gas heating mechanisms.

The SI, FeII, and SiII emission line strengths are complicated by chemistry in the disk. For disks of low gas mass ( $10^{-3} - 10^{-2} M_J$ ), the main sulfur species in the denser regions near the midplane of the disk is atomic sulfur, and sulfur is photoionized near the surface. Iron and silicon are completely ionized throughout such disks. In this low gas mass limit, the emission increases as the gas mass increases and as the dust mass increases. A higher dust mass, in general, implies more heating through gas-grain collisions and hence warmer gas. As the gas mass increases to  $0.1 M_J$  or higher, the main sulfur-bearing species near the midplane is  $SO_2$ , as sulfur turns molecular at these high densities and opacities. Here most of the atomic sulfur is in a layer above the midplane where there is enough penetration of stellar radiation to photodissociate  $SO_2$ , but not sufficient to ionize sulfur. Similarly, chemistry also affects the FeII and SiII lines, as there is substantial amounts of neutral iron and silicon in the denser regions (i.e. near the inner midplane) of the more massive disks. The SI line is optically thick for all the gas masses considered here and at higher gas masses, the line luminosity is approximately independent of mass. There is a slight increase in the line strength at  $10^{-2} M_J$  as X-rays also contribute to the gas heating making the gas warmer, and a sharp decrease at lower gas masses as sulfur gets ionized due to lower column densities. The  $[SI]25.23\mu m$  line is stronger than the  $56\mu m$  line by a factor of  $3 - 10$  in all cases. The SiII and FeII line luminosities show a similar dependence with gas mass, becoming independent of mass the lines get optically thick for gas masses  $\gtrsim 10^{-2} - 0.1 M_J$ . The emission from  $[FeI]24\mu m$ , on the other hand, increases rapidly with gas mass ( $\gtrsim 0.1 M_J$ ) due to the increased abundance of warm dense FeI gas. The  $[FeI]24\mu m$  line is the strongest line, with luminosities exceeding that of  $[SI]25.23\mu m$  for massive disks, making it an excellent tracer of gas in disks with masses  $\gtrsim 0.1 M_J$ . However, its line strength depends on the gas phase abundance of Fe in these disk regions, which is uncertain.

The  $[OI]63\mu m$  line is strong, and does not show much variation in strength with increasing gas mass, reflecting the fact that the  $[OI]$  line is nearly always optically thick. The emission is only weakly dependent on the dust mass, as it arises mostly from the surface regions of the disk where X-rays dominate the heating. The  $[OI]146\mu m$  line is weaker than the  $63\mu m$  line by approximately a factor of 10, but is strong enough to be detected in more

massive (and more dusty) disks. Emission from the [CII]158 $\mu$ m line from  $r \leq 20$  AU is too weak to be observed by Herschel or SOFIA, as the region of ionized carbon at the disk surface is too low in mass to be significant. CO emission increases with increasing gas mass. CO emission is optically thick for low J transitions and is dependent on the temperature and area of the emitting surface. The line strength increases for moderately high J transitions, whose wavelengths lie closer to the blackbody peak of the warm disk gas, and peaks at the optically thin 15  $\rightarrow$  14 transition at 187 $\mu$ m which arises mostly from within  $\sim$ 10 AU of the disk.

Emission from various lines of H<sub>2</sub>O and OH is found to be strong for disks with gas masses  $\gtrsim 0.1 M_J$ . In these disks, the densities are high and the abundance of these species is high making them strong coolants. OH is a strong coolant when the gas temperature is high ( $\sim$ few 100 K), and OH line emission mostly arises from the dense, hot inner disk where H<sub>2</sub>O photodissociates to OH more readily. Cooling by H<sub>2</sub>O dominates in the dense equatorial regions of these massive disks at all radii, but the emission is spread in various lines in the mid-IR, only some of which lie in the the Spitzer Space Telescope band from 10–37  $\mu$ m. The abundance of lines also implies that the cooling luminosity is distributed over many lines which reduces the strength of each individual line. Table 4 lists the strongest infrared line luminosities of the ortho and para-H<sub>2</sub>O species and OH for a disk with a gas mass of 0.1  $M_J$  and dust mass 10<sup>-5</sup>  $M_J$ , with all other parameters having their fiducial values.

## 5.2. Variation of Spectra with Other Parameters.

The position of the inner radial cutoff,  $r_i$  is an important parameter which can alter the observed strength of emission lines. We have run cases with four different values of this inner radius equal to 0.3, 1.0, 3.0 and 10 AU from the central star, keeping all other parameters identical to our standard disk model. Disks with smaller inner holes have a small mass of hotter, denser gas which lies closer to the central star, and might be expected to have increased line luminosities as compared to disks with large inner holes. However, larger inner holes increase the gas mass heated and chemically altered by X-rays and UV, so the situation is in fact more complicated. The fluxes for all the lines (except FeI) are seen to drop when the inner radius is decreased from 1 AU to 0.3 AU. The higher disk densities in the inner disk cause sulfur to turn molecular, and reduce the ionization of iron and silicon. With lower abundances of S, Fe<sup>+</sup> and Si<sup>+</sup> and a smaller surface area of warm gas, their line luminosities correspondingly decrease. The line luminosity from the FeI line however increases due to a higher abundance of neutral iron. The strength of the H<sub>2</sub> lines is also seen to decrease slightly, and this is due to lower masses of  $\gtrsim 100$  K H<sub>2</sub> gas for the  $r_i = 0.3$  AU disk because

of effective self-shielding from UV and X-rays. When the disk inner radius is increased from 3 AU to 10 AU, emission from all the lines except Si and H<sub>2</sub> S(0) increases again. A disk with such a large inner radius has a significantly low radial column density ( $\sim 4 \times 10^{23} \text{ cm}^{-2}$  through the midplane) so that X-rays more effectively penetrate the disk, and now dominate gas-grain collisions as the main heating mechanism. The enhanced emission in most of the lines is due to a higher gas temperature due to X-ray heating through most of the disk. Emission from the [Si] lines is seen to decrease, however, and this is because of a higher ionization rate of sulfur which lowers the atomic sulfur abundance and lowers the effective area of warm [Si] gas relative to a disk with a smaller inner disk radius.

Variations in the surface density power-law profile (Figure 13) have similar effects on the line intensities as changing  $r_i$ . The amount of warm gas in the inner regions is sensitive to the power-law index  $\alpha$ , and for a steeper power-law there is more mass in the inner region as compared to a shallower surface-density profile. We have considered three different power-law indices,  $\alpha = 0.5, 1$ , and  $1.5$ . For the largest value of  $\alpha$ , there is a decrease in the strength of the [SiII]34.8 $\mu\text{m}$  and [FeII]26 $\mu\text{m}$  lines, as the increased densities in the inner regions increase the shielding of these species from photoionization, and their abundances decrease. Correspondingly, the [FeI]24 $\mu\text{m}$  line increases sharply for large  $\alpha$ .

The X-ray luminosity of the star was taken to be  $10^{-4}$  times the bolometric luminosity in the standard case, as is typical for a weak-lined T Tauri star or more evolved stars (Feigelson et al. 2003). However, this value may be higher or lower depending on the age of the star and other factors, and we have run cases where we assume an X-ray luminosity of  $10^{-5}$  to  $10^{-3}$  times the bolometric luminosity. The X-ray spectrum is assumed to remain the same, peaking at around 2 keV and ranging from 0.5–10 keV. The X-ray luminosity has surprisingly little effect on the Spitzer Space Telescope lines as can be seen from Figure 14. The line luminosities seem largely insensitive to the amount of X-ray flux, and this can be understood by referring to the temperature structure (Figures 5 and 6) for the standard case. The X-rays only penetrate and heat a very small fraction of the mass of the disk, and in these regions, most of the heating is carried away as infrared emission from dust and by the [OI]63 $\mu\text{m}$  line. The strength of this line correlates with the X-ray flux as it comes mostly from the upper surface regions of the inner disk where the gas is warm and heated by X-rays (see Figure 6).

The infrared line emission from gas is quite sensitive to the stellar flux, with stronger emission from gas disks around more luminous stars. We have run our disk models for two different stellar types, a G2 star and a K4 star. In both cases, all disk parameters were the same, and the X-ray luminosity in both cases was  $10^{-4}$  the stellar luminosity. With lower X-rays and UV flux and with the dust grains around the less luminous K star being colder,

the gas temperature is much lower in the disk around the K4 star. Consequently, the line emission strengths are correspondingly lower (Figure 15). The [SI]25.23 $\mu$ m, [SiII]34.8 $\mu$ m, [FeII]26 $\mu$ m and the [OI]63 $\mu$ m lines may still be strong enough for detection by the Spitzer Space Telescope and SOFIA for disks at  $d \lesssim 30$  pc, especially if the X-ray luminosities are higher than average.

Lowering the minimum grain size in the dust distribution increases line emission, as can be seen from Figure 16. In our standard case, the minimum grain size,  $a_{min}$  was chosen to be 1  $\mu$ m, and we have run cases where the minimum grain size was 0.1  $\mu$ m and 10 $\mu$ m. Smaller dust grains are less efficient at re-radiating stellar radiation, and get hotter as the grain size decreases. In addition, for a fixed dust mass and  $s = 3.5$ , the grain surface area is proportional to  $a_{min}^{-1/2}$ , and therefore decreasing  $a_{min}$  increases the surface area. Both of these effects raise the gas temperature, since the gas heating is largely by gas-grain collisions and this heating rate is proportional to  $(T_{dust} - T_{gas})$  and the dust surface area. The resultant higher gas temperatures raise the total infrared line emission from the disk.

In all our models, we did not allow the formation of H<sub>2</sub> on dust grains. It is not clear if hydrogen atoms stick on warm dust grains long enough to allow the formation of H<sub>2</sub> (Cazaux & Tielens 2002) and we have run the standard model where we allow the grain formation of H<sub>2</sub>. We find that there are no significant differences in the resultant spectrum of the disk in the two cases. Even when grain formation of H<sub>2</sub> is set to zero, H<sub>2</sub> is formed efficiently by reactions with H<sup>+</sup> and by 3-body reactions.

## 6. Discussion, Summary and Conclusions

We have modeled the  $\sim$ 0.3 AU to 20 AU regions of “intermediate-aged” and “debris” disks with a range of dust masses  $10^{-7} - 10^{-4}$  M<sub>J</sub> (or  $f_D = L_{IR}/L_{bol} = 10^{-4} - 10^{-1}$ ) and gas masses  $10^{-3} - 1$  M<sub>J</sub>. We define dust as grains with size  $a \leq 1$  mm, and, assuming a size distribution  $n_{dust}(a) \propto a^{-3.5}$ , we find that these disks are reasonably optically thin to starlight for  $M_{dust} < 10^{-4}$  M<sub>J</sub>. Therefore, we have covered all of parameter space relevant to intermediate-aged and debris disks with sufficient gas and dust to be detected in IR emission lines in the next decade by observatories such as the Spitzer Space Telescope, SOFIA and Herschel.

Although the dust is optically thin to stellar photons, the gas is optically thick at UV and X-ray wavelengths. Therefore, we find that the dominant gas heating mechanism for the bulk of the gas which is shielded from heating by UV or X-rays by gas in the inner regions or at the surface, is gas-dust collisions. In these regions the dust is heated by stellar photons

and colder gas is heated by collisions with warmer dust grains. However, at the surface of the disk and at the inner edge of the disk (assuming a hole or a gap between disk and star), the UV and X-rays heat the gas, and the gas temperature can exceed the temperature of even the smallest grains. We find that the gas temperature in the 0.3 AU to 20 AU regions of debris disks range from  $\sim$ 1000K to  $\sim$ 50 K.

The chemistry in the innermost regions and at the surface of the disk is dominated by photoionization and photodissociation caused by UV and X-rays. However, in the cooler, shielded regions the chemistry is dominated, like interstellar cloud chemistry, by ion-neutral reactions with ionization by cosmic rays, UV and X-rays. We assume that at  $r \lesssim 20$  AU, the grains are too warm ( $T_{dust} \gtrsim 100$  K) to support icy mantles or to allow surface catalysis of H<sub>2</sub>. However, H<sub>2</sub> is still efficiently formed by the reaction of H with H<sup>+</sup> and by three-body reactions. In warmer regions ( $T_{gas} \gtrsim 300$  K) neutral-neutral reactions with activation barriers become important, with the general result of enhanced production of OH and H<sub>2</sub>O. In addition, the reaction of O with H<sub>2</sub> to form OH can dominate the destruction of the H<sub>2</sub> molecule. Photodissociation of molecules by UV photons play a large role in molecular destruction and creation of ions such as Fe<sup>+</sup> and Si<sup>+</sup>. We find that sulfur is S<sup>+</sup> at the disk surface, S at intermediate gas opacities, and SO<sub>2</sub> in regions well shielded by overlying gas opacity. Because H<sub>2</sub> and CO so readily self-shield and are shielded by atomic C, we find that for cases with sufficient gas mass to be detected ( $M_{gas} \gtrsim 10^{-2} M_J$ ) the bulk of hydrogen is H<sub>2</sub> and the bulk of carbon is CO in the disks. Unlike the case of interstellar clouds, the carbon becomes CO before the hydrogen becomes H<sub>2</sub> as one moves to greater depths from the disk surface, a result caused by the lack of production of H<sub>2</sub> on grain surfaces in the warm disk regions.

Surprisingly, we find that the strongest mid-IR line is [SI]25.23 $\mu$ m. This results from the high value of the product of its abundance times its spontaneous decay rate (or A-value). We find that [SI] is a strong coolant in the inner disk for all our disk models with various input parameters. We have included detailed sulfur chemistry to determine the abundance of atomic sulfur in the disk, and emission is strong enough for detection even when substantial amounts of gas has turned molecular (mainly SO<sub>2</sub>). The total mass of gas in disks is a little more difficult to obtain from measurements of the [SI]25.23 $\mu$ m line alone, as the amount of neutral atomic sulfur is affected by the chemistry of the disk. In addition, the [SI] line tends to be optically thick, and therefore not sensitive to the total gas mass.

Other strong mid-IR lines include [SiII]34.8 $\mu$ m, [FeII]26 $\mu$ m, [FeI]24 $\mu$ m and OH and H<sub>2</sub>O rotational transitions. We assume depleted gas-phase silicon and iron abundances (see Table 5, Appendix A) similar to ice-free regions of the ISM. However, we have no iron chemistry in our models other than ionization and recombination. We do include more chemistry

for silicon and consider some molecular species of Si, such as SiO and SiH<sub>2</sub>. However, the abundances of the silicon molecules are calculated to be very low, primarily because of photodissociation. In disks with low gas masses ( $M_{gas} \lesssim 10^{-2} M_J$ ), Si and Fe are ionized through most of the disk, and the line intensities we compute are probably reasonably accurate even though we do not treat the chemistry of these species in detail. In disks with higher gas masses, Si and Fe are shielded from photoionization and the [FeI]24 $\mu$ m line becomes strong. The OH and H<sub>2</sub>O lines become detectable at relatively high gas masses,  $M_{gas} \gtrsim 10^{-2} M_J$ .

Pure rotational H<sub>2</sub> lines such as S(0) 28  $\mu$ m and S(1) 17  $\mu$ m are roughly an order of magnitude weaker than the [SI]25.23 $\mu$ m line. The highest spectral resolving power of the Spitzer Space Telescope is  $R \sim 600$ , and this modest resolution makes it difficult to detect weak mid-IR (10–37  $\mu$ m) lines in the presence of strong(dust) mid-IR continuum. Detection of the relatively weak H<sub>2</sub> lines above the dust continuum requires a relatively large ratio ( $\gtrsim 1000$ ) of gas mass to dust mass. Such large ratios are possible at a transition epoch ( $\sim 10^7$  years) where much of the dust mass has coagulated into particles of sizes  $a \gg 1$  mm, but the gas has not yet appreciably dispersed.

Most of the Spitzer Space Telescope high spectral resolution emission arises from gas at  $r \lesssim 5$  AU in our models, whereas longer wavelength (lower excitation) emission such as from low to mid-J CO lines and OI 63  $\mu$ m has significant contribution from gas at  $r \gtrsim 5$  AU. The OI line arises from the entire disk and is a good probe of the conditions throughout the disk. While the mid-IR lines observable by the Spitzer Space Telescope are insensitive to the strength of the X-ray flux, the intensity of the [OI]63 $\mu$ m line does increase with the X-ray luminosity. SOFIA is capable of observing this transition, and may be able to detect smaller amounts of gas in disks around stars that are strong X-ray sources. Our models indicate that CO emission is strong enough to be detectable and it is a strong coolant in the outer cold regions of the disk. CO line luminosities are  $\sim 10^{-9} L_\odot$  in the  $2 \rightarrow 1$  line, and  $\sim 10^{-7} L_\odot$  in the higher  $15 \rightarrow 14$  transition for our fiducial disk. Higher J transitions of CO in the far-infrared and the sub-millimeter wavelength regions can be easily detected by Herschel and can reveal the extent of the gas disk.

Line ratios are also diagnostic of the gas characteristics. The [FeI]24 $\mu$ m line is only strong when there is high shielding (or high columns and densities) in the inner disk regions. This requires either high gas masses, steep surface density distributions, small inner holes, or a combination of these. The FeI/SI ratio is especially suited to probing these parameters. Significant amounts of [OI]63 $\mu$ m and CO ( $J = 15 \rightarrow 14$ ) 187  $\mu$ m radiation emanate from regions  $r \gtrsim 5$  AU, in contrast to the SI or H<sub>2</sub> 17  $\mu$ m lines. Therefore, the ratios [OI]63 $\mu$ m/SI, [OI]63 $\mu$ m/H<sub>2</sub> 17  $\mu$ m, CO 187  $\mu$ m/H<sub>2</sub> 17  $\mu$ m are sensitive to the relative masses of gas at  $r \lesssim 5$  AU compared to that at  $r \gtrsim 5$  AU. In other words, these ratios are sensitive to the

steepness of the surface density distribution.

The overall strength of the mid-IR lines primarily depends on the mass of warm ( $T \gtrsim 100$  K) gas, which typically lies within 5 AU of the central star. Disks with more total gas mass, with smaller inner holes, or with steeper surface density distributions, produce stronger mid-IR emission. Because gas-dust collisions mainly heat the bulk of the gas, the line emission also increases with either greater dust mass, or, holding dust mass fixed, with smaller minimum grain size  $a_{min}$ . In the latter case, the smaller size grains are warmer and have greater surface area than their larger counterparts, and therefore heat the gas more vigorously.

As little as  $10^{-3}M_J$  of warm gas at  $r \lesssim 5$  AU can be detected by the Spitzer Space Telescope in the [SI]25 $\mu$ m line for sources at  $\sim 30$  pc from the Sun. However, to better diagnose the physical characteristics of the gas requires the detection of several lines, and this requires roughly an order of magnitude greater gas mass ( $\sim 10^{-2} M_J$ ) at this distance. We emphasize that the line luminosities in the strongest lines ([SI], [SiII], [FeII] and [OI]) increase very slowly or even decrease with increasing gas mass (see Fig. 10). This is because the gas temperature in these disks is largely controlled by the dust temperature, which is independent of gas mass, and the gas emission lines at high gas mass become optically thick so that their luminosities saturate. Our results show that at the distance of Taurus (140 pc), even  $1 M_J$  of gas in intermediate-aged optically thin dust disks could be difficult to detect. However, typical disks in Taurus are more likely to be younger and therefore abundant in small grains ( $a_{min} \sim 50\text{\AA}$ ). A younger central star is also more luminous in FUV. This will lead to an increase in both collisional gas-grain heating (due to the larger surface area of small grains) and grain photoelectric heating which will make the gas warmer and increase gas line emission significantly.

Assuming that we know the distance to the source, the X-ray and FUV luminosities of the central star, and the dust mass and dust distribution from the IR and sub-mm/millimeter continuum observations, we can readily constrain the gas properties by comparing the observed fluxes in various emission lines with our models. Ultimately, if the lines are spectrally resolved by high resolution instruments on SOFIA or Herschel, the line profiles will also help constrain the gas dynamics and spatial distribution.

To conclude, we find exciting prospects for the detection by the Spitzer Space Telescope, SOFIA or Herschel of infrared line emission from the gas in 0.3 AU to 20 AU regions of intermediate-aged disks at distances  $\lesssim 150$  pc. The core accretion model of giant planet formation strongly suggests an epoch ( $t < 10^{6.5} - 10^7$  years) when the dust in the 1 AU–20AU region is relatively optically thin, due to the growth of several earth-mass cores, but where  $\gtrsim 1 M_J$  of gas persists for an extended period. Therefore, the observations of line emission coupled with the models presented here will provide a measure of the evolution of

gas in disks as they transition from planet-forming disks to the older, gas-free, debris disks and a test of the core-accretion scenario for gas giant planet formation. The presence of even small amounts of gas at times  $t \sim 10^7$  to  $10^8$  years has important effects on planet formation in the 0.3-20 AU region.

We acknowledge very helpful discussions with all the members of the Formation and Evolution of Planetary Systems (FEPS) Spitzer Legacy team, especially John Carpenter, Michael Meyer, Joan Najita, Deborah Padgett, Stu Weidenshilling and Sebastian Wolf. We also acknowledge helpful advice from Al Glassgold and Inga Kamp. Support for this work comes from the NASA FEPS SIRTF Legacy grant and a NASA Origins of Solar Systems grant.

## REFERENCES

Adams, F.C., Shu, F.H., Lada, C.J., 1988, ApJ, 326, 865  
Adams, F.C., Hollenbach, D.J., Laughlin, G., Gorti, U., 2004, ApJ, submitted  
Agnor, C.B., Ward, W.R., 2002, ApJ, 567, 579  
Aikawa, Y., Umebeyashi, T., Nakano, T., Miyama, S., 1999, ApJ, 519, 705  
Aikawa, Y., van Zadelhoff, G.J., van Dishoeck, E.F., Herbst, E., 2002, A&A, 386, 622  
Ayres, T.R. 1997, JGR, 102, 1641  
Backman, D.E., Paresce, F., 1993, Protostars and Planets III, 1253  
Bakes, E., Tielens, A.G.G.M., 1994, ApJ, 427, 822  
Balbus, S., Hawley, J.F., 1991, ApJ, 376, 214  
Brandeker, A., Liseau, R., Olofsson, G., Fridlund, M. 2004, A&A, 413, 681  
Beckwith, S.V.W., Sargent, A.I. 1996, Nature, 383, 139  
Bell, K.R., Cassen, P.M., Klahr, H.H., Henning, Th., 1997, ApJ, 486, 372  
Boss, A., 2003, ApJ, 599, 577  
Burke, J.R., Hollenbach, D.J., 1983, ApJ, 265, 223  
Calvet, N., D'Alessio, P., Hartmann, L., et al. 2002, ApJ, 568, 1008  
Cazaux, S., Tielens, A.G.G.M., 2002, ApJ, 575, 29  
Chiang, E., Goldreich, P., 1997, ApJ, 490, 368  
Clarke, C.J., Gendrin, A., Sotomayor, M., 2001, MNRAS, 328, 485

D'Alessio, P., Canto, J., Calvet, N., Lizano, S., 1998, *ApJ*, 500, 411

D'Alessio, P., Calvet, N., Hartmann, L., et al. 1999, *ApJ*, 529, 893

Draine, B.T., 1978, *ApJS*, 36, 595

Draine, B.T., Bertoldi, F. 1996, *ApJ*, 468, 269

Dullemond, C.P. 2002, *A&A*, 395, 853

Dullemond, C.P., van Zadelhoff, G.J., Natta, A., 2002, *A&A*, 389, 464

Dullemond, C.P., Dominik, C., Natta, A., 2001, *ApJ*, 560, 957

Dutrey, A., Guilloteau, S., Duvert G., et al., 1996, *A&A*, 309, 493

Duvert G., Guilloteau, S., Menard, F., et al. 2000, *A&A*, 355, 165

Feigelson, E.D., Montmerle, T., 1999, *ARA&A*, 37, 363

Feigelson, E.D., Gaffney, J.A., Garmire, G., et al. 2003, *ApJ*, 584, 911

Glassgold, A., Najita, J., Igea, J., 1997, *ApJ*, 485, 920

Glassgold, A., Najita, J., Igea, J., 2004, in preparation

Habing, H.J., 1968, *Bull. Astron. Inst. Netherlands*, 19, 421

Habing, H.J., Dominik, C., Jourdain de Muizon, M. et al. 1999, *Nature*, 401, 456

Haisch, K.E., Lada, E.A., Lada, C.J., 2001, *ApJ*, 553, 153

Henning, Th., Il'In, V.B., Krivova, N.A., et al. 1999, *A&AS*, 136, 405

Hollenbach, D.J., Salpeter, E., 1971, *ApJ*, 163, 155

Hollenbach, D.J., McKee, C.F., 1979, *ApJS*, 41, 555

Hollenbach, D.J., Johnstone, D., Lizano, S. Shu F., 1994, *ApJ*, 428, 654

Hollenbach, D.J., Yorke, H.W., Johnstone, D. 2000, *Protostars and Planets IV*, 404

Ilgner, M., Henning, Th., Markwick, A.J., Millar, T.J., 2004, *A&A*, 415, 643

Johnstone, D., Hollenbach, D.J., Bally, J. 1998, *AJ*, 116, 293

Kamp, I., van Zadelhoff, G.J., 2001, *A&A*, 373, 641

Kamp, I., Sammar, F., 2003, in *Stars as Suns: Activity, Evolution and Planets*, IAU Symp. No. 219, p106

Kaufman, M.J., Wolfire, M.G., Hollenbach, D., Luhman, M.L., 1999, *ApJ*, 527, 795

Klahr, H.H., Lin, D.N.C., 2001, *ApJ*, 554, 1095

Kominami, J., Ida, S., 2002, *Icarus*, 157, 43

Kominami, J., Ida, S., 2004, *Icarus*, 167, 231

Kornet, K., Bodenheimer, P., Rozyczka, M., 2002, *A&A*, 396, 977

Lagrange, A-M., Backman, D., Artymowicz, P., *Protostars and Planets IV*, 2000, 639

Lauchame, R., Malbet, F., Monin, J-L., 2003, *A&A*, 400, 185

Lecavalier des Etangs, A., Vidal-Madjar, A., Roberge, A., et al. 2001, *Nature*, 412, 706

Le Teuff, Y.H., Millar, T.J., Markwick, A.J., 2000, *A&AS*, 146, 157

Li, A., Greenberg, J.M., 1998, *A&A*, 331, 291

Lissauer, J., 1993, *ARA&A*, 31, 129

Liu, M.C., Matthews, B.C., Williams, J.P., Kalas, P.G., 2004, *ApJ*, in press

Lynden-Bell, D., Pringle, J., 1974, *MNRAS*, 168, 603

Markwick, A.J., Ilgner, M., Millar, T.J., Henning, Th., 2002, *A&A*, 385, 632

Maloney, P.R., Hollenbach, D., Tielens, A.G.G.M., 1996, *ApJ*, 466, 561

Natta, A., Prusti, T., Neri, R. et al. 2001, *A&A*, 371, 186

Natta, A., Testi, L., Neri, R., Shepherd, D.S., Wilner, D.J., 2004, *A&A*, 416, 179

Pollack, J., Hubickyj, O., Bodenheimer, P., Lissauer, J., Podolak, M., Greenzweig, Y., 1996, *Icarus*, 124, 62

Richter, M.J., Jaffe, D.T., Blake, G.A., Lacy, J.H., 2002 *ApJ* 572, 161

Savage, B.D., Sembach, K.R., 1996, *ApJ*, 470, 893

Shakura, N.I., Sunyaev, R.A. 1973, *A&A*, 24, 337

Shang, H., Glassgold, A., Shu, F., Lizano, S., 2002, *ApJ*, 564, 853

Sheret, I., Ramsay Howat, S.K., Dent, W.R.S., 2003, *MNRAS*, 343, 65

Shull, J.M., van Steenberg, M. 1985, *ApJ*, 294, 599

Spangler, C., Sargent, A.I., Silverstone, M.D., et al. 2001, *ApJ*, 555, 932

Takeuchi, T., Artymowicz, P. 2001, *ApJ*, 557, 990

Takeuchi, T., Lin, D.N.C., 2002, *ApJ*, 581, 1344

Thi, W.F., Blake, G.A., van Dishoeck, E.F. et al. 2001, *Nature*, 409, 60

Throop, H.B., Bally, J., Esposito, L.W., McCaughrean, M., 2001, *Science*, 292, 1686

Tielens, A.G.G.M., Hollenbach, D., 1985, *ApJ*, 291, 722

Weidenschilling, S.J., Spaute, D., Davis, D.R., et al. 1997, *Icarus*, 128, 429

Weidenschilling, S.J. 1977, MNRAS, 180, 57

Watson, W.D., 1972, ApJ, 176, 103

Weingartner, J.C., Draine, B., 2001, ApJS, 134, 263

Willacy, K., Klahr, H.H., Millar, T.J., Henning, Th. 1998, A&A, 338, 995

Wilms, J., Allen, A., McCray, R., 2000, ApJ, 542, 914

Wolk, S.J., Walter, F.M., 1996, AJ, 111, 2066

van Dishoeck, E.F., Black, J.H., 1988, ApJ, 334, 711

Verner, D.A., Yakovlev, D.G., 1995, A&A, 109, 125

Zuckerman, B., Forveille, T., Kastner, J.H. 1995, Nature, 373, 494

Zuckerman, B. 2001, ARA&A, 39, 549

Table 1: Input Parameters for Standard Disk Model

Gas mass	$10^{-2} M_J$	Dust mass	$10^{-5} M_J$
Inner radius $r_i$	1 AU	Minimum grain size $a_{min}$	$1.0 \mu\text{m}$
Outer radius $r_o$	20 AU	Maximum grain size $a_{max}$	1.0 mm
Surface density power law index $\alpha$	1.0	Grain size dist. index $s$	3.5
Stellar age (for FUV flux)	$10^7$ years	Grain composition	Am. Olivine
Stellar X ray Luminosity	$4.0 \cdot 10^{29} \text{ erg s}^{-1}$	Stellar bol. luminosity	$4.0 \cdot 10^{33} \text{ erg s}^{-1}$
Stellar temperature $T_*$	5780 K		

Table 2: Infrared Emission Lines, their Wavelengths and Observing Instruments.

Species	$\lambda(\mu\text{m})$	Transition	Telescope instruments
H <sub>2</sub> S(2)	12.3		Spitzer IRS, SOFIA EXES
H <sub>2</sub> S(1)	17.0		Spitzer IRS, SOFIA EXES
H <sub>2</sub> S(0)	28.2		Spitzer IRS, SOFIA EXES
OH	15-200		Spitzer IRS, SOFIA EXES, GREAT, SAFIRE, Herschel SPIRE
H <sub>2</sub> O	15-200		Spitzer IRS, SOFIA EXES, GREAT, SAFIRE, Herschel SPIRE
FeI	24.0	<sup>5</sup> D <sub>3</sub> – <sup>5</sup> D <sub>4</sub>	Spitzer IRS, SOFIA EXES
Si	25.2	<sup>3</sup> P <sub>1</sub> – <sup>3</sup> P <sub>2</sub>	Spitzer IRS, SOFIA EXES
FeII	26.0	<sup>6</sup> D <sub>7/2</sub> – <sup>6</sup> D <sub>9/2</sub>	Spitzer IRS, SOFIA EXES
SiII	34.8	<sup>2</sup> P <sub>3/2</sub> – <sup>2</sup> P <sub>1/2</sub>	Spitzer IRS
FeI	34.2	<sup>5</sup> D <sub>2</sub> – <sup>5</sup> D <sub>3</sub>	Spitzer IRS
FeII	35.4	<sup>6</sup> D <sub>5/2</sub> – <sup>6</sup> D <sub>7/2</sub>	Spitzer IRS
Si	56.6	<sup>3</sup> P <sub>0</sub> – <sup>3</sup> P <sub>1</sub>	SOFIA FIFI-LS
OI	63.1	<sup>3</sup> P <sub>1</sub> – <sup>3</sup> P <sub>2</sub>	SOFIA FIFI-LS, GREAT, Herschel PACS
OI	145.6	<sup>3</sup> P <sub>0</sub> – <sup>3</sup> P <sub>1</sub>	SOFIA SAFIRE, GREAT, Herschel SPIRE
CII	157.7	<sup>2</sup> P <sub>3/2</sub> – <sup>2</sup> P <sub>1/2</sub>	SOFIA SAFIRE, GREAT, Herschel SPIRE
CI	369.0	<sup>3</sup> P <sub>2</sub> – <sup>3</sup> P <sub>1</sub>	SOFIA CASIMIR, SAFIRE, Herschel HIFI
CI	609.2	<sup>3</sup> P <sub>1</sub> – <sup>3</sup> P <sub>0</sub>	SOFIA SAFIRE, Herschel HIFI

Table 3: Parameter Range for Disk Model

Gas mass	$10^{-3} - 1 M_J$	Dust mass	$10^{-7} - 10^{-4} M_J$
Inner radius $r_i$	0.3-10 AU	Minimum grain size $a_{min}$	$0.1-10.0 \mu\text{m}$
Outer radius $r_o$	20 AU	Maximum grain size $a_{max}$	1.0 mm
Surface density power law index $\alpha$	0.5-2.0	Grain size dist. index $s$	3.5
Stellar X ray Luminosity	$10^{-2} - 10^{-5} L_{bol}$	Stellar temperature $T_*$	4500K and 5780 K

Table 4: Line luminosities of OH and H<sub>2</sub>O lines for a disk with a gas mass of 0.1 M<sub>J</sub> and dust mass 10<sup>-3</sup> M<sub>J</sub>, with all other parameters at their fiducial values.

Species	$\lambda(\mu\text{m})$	Line lum. (in L <sub>⊙</sub> )	Species	$\lambda(\mu\text{m})$	Line lum. (in L <sub>⊙</sub> )
OH	30.54	9.8×10 <sup>-8</sup>	OH	30.63	1.0×10 <sup>-7</sup>
OH	33.80	1.4×10 <sup>-7</sup>	OH	33.93	1.4×10 <sup>-7</sup>
OH	37.01	1.8×10 <sup>-7</sup>	OH	37.08	1.8×10 <sup>-7</sup>
OH	38.84	7.7×10 <sup>-7</sup>	OH	38.88	6.5×10 <sup>-7</sup>
o-H <sub>2</sub> O	21.15	2.6×10 <sup>-7</sup>	p-H <sub>2</sub> O	21.17	2.6×10 <sup>-7</sup>
p-H <sub>2</sub> O	21.18	3.0×10 <sup>-7</sup>	p-H <sub>2</sub> O	21.83	2.8×10 <sup>-7</sup>
o-H <sub>2</sub> O	21.85	3.1×10 <sup>-7</sup>	p-H <sub>2</sub> O	21.89	2.7×10 <sup>-7</sup>
p-H <sub>2</sub> O	23.19	3.0×10 <sup>-7</sup>	o-H <sub>2</sub> O	23.90	3.2×10 <sup>-7</sup>
o-H <sub>2</sub> O	25.17	2.9×10 <sup>-7</sup>	p-H <sub>2</sub> O	25.22	3.1×10 <sup>-7</sup>
o-H <sub>2</sub> O	25.94	4.0×10 <sup>-7</sup>	p-H <sub>2</sub> O	25.98	3.1×10 <sup>-7</sup>
p-H <sub>2</sub> O	27.03	3.1×10 <sup>-7</sup>	o-H <sub>2</sub> O	27.99	3.1×10 <sup>-7</sup>
o-H <sub>2</sub> O	28.59	2.7×10 <sup>-7</sup>	p-H <sub>2</sub> O	28.59	2.7×10 <sup>-7</sup>
p-H <sub>2</sub> O	28.91	2.3×10 <sup>-7</sup>	p-H <sub>2</sub> O	29.36	2.7×10 <sup>-7</sup>
o-H <sub>2</sub> O	29.84	3.0×10 <sup>-7</sup>	p-H <sub>2</sub> O	29.88	2.9×10 <sup>-7</sup>
p-H <sub>2</sub> O	30.47	2.6×10 <sup>-7</sup>	p-H <sub>2</sub> O	30.53	2.7×10 <sup>-7</sup>
o-H <sub>2</sub> O	30.53	2.8×10 <sup>-7</sup>	o-H <sub>2</sub> O	30.87	2.5×10 <sup>-7</sup>
o-H <sub>2</sub> O	30.90	3.4×10 <sup>-7</sup>	p-H <sub>2</sub> O	31.74	2.5×10 <sup>-7</sup>
p-H <sub>2</sub> O	33.00	2.9×10 <sup>-7</sup>	o-H <sub>2</sub> O	33.01	3.0×10 <sup>-7</sup>
p-H <sub>2</sub> O	34.40	2.0×10 <sup>-7</sup>	o-H <sub>2</sub> O	34.55	2.7×10 <sup>-7</sup>
o-H <sub>2</sub> O	35.43	2.7×10 <sup>-7</sup>	p-H <sub>2</sub> O	35.47	3.2×10 <sup>-7</sup>
o-H <sub>2</sub> O	35.67	2.2×10 <sup>-7</sup>	p-H <sub>2</sub> O	35.90	2.9×10 <sup>-7</sup>
p-H <sub>2</sub> O	36.21	2.7×10 <sup>-7</sup>	o-H <sub>2</sub> O	66.44	2.6×10 <sup>-7</sup>
o-H <sub>2</sub> O	75.38	3.6×10 <sup>-7</sup>	p-H <sub>2</sub> O	100.98	8.1×10 <sup>-7</sup>
o-H <sub>2</sub> O	108.07	3.3×10 <sup>-7</sup>	p-H <sub>2</sub> O	138.53	5.9×10 <sup>-7</sup>
o-H <sub>2</sub> O	179.53	2.2×10 <sup>-7</sup>			

## A. Chemistry

We adopt gas phase abundances from Savage & Sembach (1996) towards the line of sight through a diffuse cloud to the star  $\zeta$  Oph. The abundances are listed in Table 5. Table 6 lists the atomic, ionic and molecular species included in our chemical code. Reaction rates are mostly from the UMIST'99 database, except for some reactions which are listed in Table 7. Apart from those listed here, X-ray photoionization rates are calculated as described in §D.3, and reactions involving PAHs and vibrationally-excited H<sub>2</sub> are from TH85. The UV photoionization rates of atoms and molecules are calculated using their photoabsorption cross sections multiplied by the stellar flux and integrated over frequency.

## B. X-ray Heating and Chemistry

### B.1. X-ray Spectrum

The stellar X-ray spectrum is assumed to be similar in form to the wTTS in Figure 2 of Feigelson & Montmerle (1999). A broken power law is fit to the data for the counts  $G$ (in counts s<sup>-1</sup> keV<sup>-1</sup>) within the energy range 0.5-10 keV, which then gives the luminosity in erg s<sup>-1</sup> keV<sup>-1</sup>,  $L(E) = G(E)E$ .

$$L(E) = 1.2L_X E^{-1.75} (E > 2\text{keV}) \quad (\text{B1})$$

$$= 0.18L_X E (E < 2\text{keV}) \quad (\text{B2})$$

$$(\text{B3})$$

where  $L_X$  is the total X-ray luminosity of the star in erg s<sup>-1</sup>, and the energy  $E$  is expressed in keV. The X-ray energy flux is given by  $F(E) = L(E)/4\pi D^2$ , where  $D = (r^2 + z^2)^{1/2}$  is the distance from a point in the disk to the star. The heating due to X-rays is

$$H_X = \int_{0.5}^{10} F(E) e^{-\tau_X} \sigma(E) n_H f_h dE \text{ erg cm}^{-3} \text{ s}^{-1} \quad (\text{B4})$$

where  $\sigma(E)$  is the total gas X-ray photoabsorption cross section per H nucleus,  $\tau_X$  is the X-ray optical depth given by  $\sigma(E)N_H$ ,  $N_H$  is the total column density of the gas towards the source,  $n_H$  is the number density and  $f_h$  is the fraction of absorbed energy that goes into heating the gas. We also include secondary heating of X-rays due to photoionization from the  $n = 2$  state of atomic hydrogen and follow exactly the treatment of Shang et al.(2002).

## B.2. X-ray Photoabsorption Cross Section $\sigma(E)$

We use the model of Wilms et al. (2000) for the X-ray photoabsorption cross section per H nucleus. They obtain the total photoionization cross section of the ISM by summing the cross sections of the gas, molecules and grains. They use cosmic abundances for the various elements, and add the contribution from grains. Our grains are large and typical X-ray penetration depths are  $\sim 0.1\mu\text{m}$ , and therefore X-rays do not penetrate even our smallest dust grains. We use only the gas-phase abundances in our calculation of the cross-section, and we adopt abundances from Savage & Sembach (1996) through a diffuse cloud towards the star  $\zeta$  Oph. We correct Figure 1 of Wilms et al.(2000) to correspond to our depleted abundances and then fit a power law to find the absorption cross section. We obtain

$$\sigma(E) = 1.2 \times 10^{-22} \left( \frac{E}{1\text{keV}} \right)^{-2.594} \quad (\text{B5})$$

Compare to the fit to the Wilms et al.(2000) cross-section

$$\sigma(E) = 2.27 \times 10^{-22} \left( \frac{E}{1\text{keV}} \right)^{-2.485} \quad (\text{B6})$$

## B.3. X-ray Photoionization Rates of Atoms and Molecules

The absorption cross section of a species  $i$  for ionization is approximated to be of the functional form

$$\sigma_i(E) = \sigma_{0i} \left( \frac{E}{1\text{keV}} \right)^\alpha$$

We use the partial photoionization cross sections of Verner & Yakovlev (1995) and the fitting formulae they provide (Table 1 of their paper). These formulae for the cross sections in the range 0.5-10 keV are then fit again with a power law of the above form for each neutral atomic species. In some cases, the cross section is fit with a broken power law within this range. Table 8 lists the values of  $\sigma_{0i}$  in barns,  $\alpha$  and the energy ranges in keV where the fits are valid. The primary rate of photoionization is given by the integral of the photon number flux and the cross section

$$\zeta_i = 6.25 \times 10^8 \int_{0.5}^{10} \sigma_i(E) \frac{F(E)}{E} e^{-\tau_X(E)} dE \text{ s}^{-1}$$

where  $F(E)$  is in units of  $\text{erg s}^{-1} \text{keV}^{-1}$ , and the energy  $E$  is in keV. The attenuation factor  $\tau_X$  has the same definition as before and is equal to the product of the *total* photoabsorption cross section and the column density towards the source.

Secondary ionizations are important for hydrogen and helium. The fraction of primary electron energy going into secondary ionization is (Shull & van Steenberg 1985),

$$\Phi_H = 0.391 \left( 1 - \frac{13.6}{E}^{0.41} \right)^{1.76} \approx 0.35$$

$$\Phi_{He} = 0.0554 \left( 1 - \frac{24.6}{E}^{0.46} \right)^{1.66} \approx 0.05$$

where  $E$  is now in eV. The number of secondary photoionizations produced by a primary electron of energy  $E$  is equal to  $E\Phi_H/13.6$  and  $E\Phi_{He}/24.6$  for hydrogen and helium. The number of secondary ionizations by a photon of energy  $E$  is therefore  $25.7(E/1\text{keV})$  for hydrogen and  $2.0(E/1\text{keV})$  for helium. The total photoionization rate for hydrogen and helium are therefore,

$$\zeta_{T,H} = 6.25 \times 10^8 \int_{0.5}^{10} \sigma_i(E) \frac{F(E)}{E} e^{-\tau_X(E)} (1 + 25.7E) dE \text{ s}^{-1}$$

$$\zeta_{T,He} = 6.25 \times 10^8 \int_{0.5}^{10} \sigma_i(E) \frac{F(E)}{E} e^{-\tau_X(E)} (1 + 2.0E) dE \text{ s}^{-1}$$

where  $E$  is in units of keV. We ignore secondary ionizations of all other species. Photoionization rates of molecules are assumed to be the sum of the rates of their constituent atoms, e.g.,  $\zeta_{OH} = \zeta_O + \zeta_H$  etc. These integrals are numerically evaluated for each species with the expressions for the cross sections and the X-ray flux, as a function of column  $N_H$  towards the star.

### C. Gas Heating Mechanisms

**Gas-grain collisions** Dust grains in the optically thin disk are heated by the stellar radiation field and collisional gas-grain energy transfer is often the dominant heating mechanism for the gas. The dust grain temperature is size-dependent, smaller grains are less efficient at re-radiating stellar light and are thus warmer than larger grains. Collisions of gas molecules with dust grains can either heat or cool the gas, depending on the gas and dust grain temperatures. Our treatment is similar to that of Hollenbach & McKee (1979, hereafter HM79) but adapted for an arbitrary grain size distribution. The net heating (or cooling) due to collisions is given by

$$\Gamma_1 = \alpha_T n_H v_{gas} \sum_{a_{min}}^{a_{max}} \pi a^2 n_{dust}(a) (2k_B T_{dust}(a) - 2k_B T_{gas}) \text{ ergs cm}^{-3} \text{ s}^{-1} \quad (\text{C1})$$

where  $\alpha_T \approx 0.3$  is the thermal accommodation coefficient (Burke & Hollenbach 1983),  $n_H$  the gas hydrogen nucleus number density,  $v_{gas}$  the thermal velocity of the gas,  $a$  the dust grain radius, that ranges from  $a_{min}$  to  $a_{max}$ ,  $n_{dust}(a)$  the number density of particles of size  $a$ , and  $T_{dust}(a)$  and  $T_{gas}$  are the temperatures of a dust grain of size  $a$  and the gas respectively.

**FUV pumping of  $H_2$  and collisional de-excitation**  $H_2$  molecules absorb FUV photons from the star and from the ISRF and are excited to a higher vibrational state. Subsequent de-excitation by collisions with H atoms and ground state  $H_2$  molecules deposits the excess energy as heat into the gas.  $H_2$  molecules can also be directly photodissociated from the vibrationally excited state, which again leads to heating. (See TH85 for a detailed discussion). The heating due to FUV pumping and collisional de-excitation is given by

$$\begin{aligned} \Gamma_2 = & 3.18 \times 10^{-12} n(H_2^*) (10^{-12} T^{0.5} \exp(-1000/T) n(H) + \\ & 1.4 \times 10^{-12} T^{0.5} \exp(-18100/(T + 1200)) n(H_2)) + \\ & G_{11.26} (1.36 \times 10^{-23} (n(H_2) \beta_1(\tau) n(H_2^*)) \beta_2(\tau)) + \\ & 5.8 \times 10^{-24} n(H_2^*) \text{ ergs cm}^{-3} \text{ s}^{-1} \end{aligned} \quad (C2)$$

where  $n(H_2)$  and  $n(H_2^*)$  are the number densities of  $H_2$  and vibrationally excited  $H_2$  respectively,  $\beta_1(\tau)$  and  $\beta_2(\tau)$  the corresponding self-shielding factors and  $G_{11.26}$  is the local photon energy flux in the range  $11.26 - 13.6 eV$  (from the star and the ISRF, attenuated by dust and other gas species), normalized to the Habing flux in the same band ( $2.26 \times 10^{-4} \text{ erg cm}^{-2} \text{ s}^{-1}$ ). We use self-shielding factors for CO from van Dishoeck & Black (1988) and for  $H_2$  from Draine & Bertoldi (1996).

**X-ray heating** X-rays incident on gas photoionize atoms and molecules, and the primary electrons thereby generated are energetic enough to cause multiple secondary ionizations. The heating term arises from the thermalization of some of the energy of these secondary electrons, and is proportional to the ionization rate due to X-rays. The heating due to X-rays is given by

$$\Gamma_3 = \int_{E_{min}}^{E_{max}} F(E) e^{-N_H \sigma(E)} \sigma(E) n_H f_h dE \text{ ergs cm}^{-3} \text{ s}^{-1} \quad (C3)$$

where  $F(E)$  is the X-ray photon flux,  $N_H$  is the hydrogen nucleus column density of gas towards the source,  $\sigma(E)$  is the X-ray absorption cross section of the gas per hydrogen nucleus (see Appendix B), and  $f_h$  is the fraction of energy that is converted to heat, equal to 0.1 for atomic gas and 0.4 for molecular gas. (See Maloney et al. 1996 for details.) We also include indirect heating by X-rays due to atomic hydrogen ionization, the recombining  $H^+$  resulting in a substantial  $n = 2$  population of H because of the trapping of Lyman  $\alpha$

photons, followed by photoionization or collisional de-excitation of  $n = 2$  hydrogen atoms. (See Shang et al. 2002.) We ignore X-ray scattering from the surface layer into the disk, as we estimate the contribution from this process to be negligible.

**Grain photoelectric heating** Energetic electrons emitted from dust grains due to the absorption of stellar FUV photons can collide with and heat the gas (Bakes & Tielens 1994). The efficiency of this process is dependent on the size of the dust grain and decreases with increasing grain size. As we consider large dust grains in our disk models, this process is not as efficient as in the ISM where small submicron sized dust grains are abundant. The grain photoelectric heating term has been revised to include the effects of a cooler radiation field (stars of lower spectral type) and increased grain sizes. We use corrected grain photoelectric efficiencies from Weingartner & Draine (2001) and Weingartner (2002, private communication) for our calculations of grain photoelectric heating in disks.

$$\Gamma_4 = G_0 \sum_{a_{min}}^{a_{max}} n_{dust}(a) \pi a^2 \epsilon(T_{FUV}, a) \text{ ergs cm}^{-3} \text{ s}^{-1} \quad (\text{C4})$$

where  $\epsilon$  is the photoelectric heating efficiency and is a function of the grain size  $a$ , the equivalent blackbody temperature of the stellar FUV flux  $T_{FUV}$ , and  $G_0$  and  $n_e$  (which determine the grain charge). The FUV flux spectrum from the star (Figure 1) has a characteristic temperature  $T_{FUV} \sim 10,000$  K.  $G_0$  is the local stellar flux between 6.0–13.6 eV, normalized to the Habing flux. A similar term for the ISRF is also included, where  $T_{FUV}$  is replaced by the temperature of the ISRF, 30000 K, although this contribution is generally negligible.

**Drift heating** Dust grains and gas molecules are subject to different forces in the disks, with radiation pressure acting only on dust and gas being constrained by thermal pressure gradients. They could have different disk velocities and orbits, and this causes a viscous heating term which could be important in dense disks (Kamp & van Zadelhoff 2001, Takeuchi and Artymowicz 2002). We add drift heating to our disk models, though we do not solve for the disk orbital dynamics of the dust or gas. The heating due to drift is given by

$$\Gamma_5 = 0.5 \mu_H n_H \sum_{a_{min}}^{a_{max}} n_{dust}(a) \pi a^2 v_{drift}^3(a) \text{ ergs cm}^{-3} \text{ s}^{-1} \quad (\text{C5})$$

where  $v_{drift}(a)$  is the drift velocity between gas and a dust particle of size  $a$ . We use the equations of Takeuchi and Artymowicz (2002) for the calculation of the drift velocity.

**Heating due to formation of  $H_2$**  We include heating due to the formation of  $H_2$  in our model. The formation of  $H_2$  either on grain surfaces or by reactions of  $H$  atoms with  $H^-$  leads to heating of the gas. The grain formation mechanism provides  $\sim 0.2$  eV of kinetic energy going into the newly formed  $H_2$  molecule, and  $\sim 4.2$  eV of energy initially deposited as rovibrational internal energy of the molecule (Hollenbach, Werner & Salpeter 1971). The reaction with  $H^-$  is an exothermic reaction which liberates  $\sim 3.53$  eV of energy and we assume that most of this energy is initially in rovibrational internal energy of the molecule. Generally in disks, the gas densities are much greater than the critical density  $n_{cr}$  to de-excite the vibrationally excited  $H_2$  molecule. Therefore, the rovibrational energy is quickly converted into heat. Grain formation of  $H_2$  is not included in our standard runs, and this heating mechanism is only included for the case where we allow formation of  $H_2$  on grains. Heating due to formation of  $H_2$  by  $H^-$  is given by

$$\Gamma_6 = 7.34 \times 10^{-21} \frac{n_H^2 x(H^-) x(H)}{1 + n_{cr}/n_H} \text{ ergs cm}^{-3} \text{ s}^{-1} \quad (\text{C6})$$

where

$$n_{cr} = \frac{10^6 T^{-1/2}}{1.6x(H) \exp[-(400/T)^2] + 1.4x(H_2) \exp[-12000/(T + 1200)]} \text{ cm}^{-3} \quad (\text{C7})$$

and  $x(H)$ ,  $x(H^-)$ , and  $x(H_2)$  are the abundances of  $H$ ,  $H^-$  and  $H_2$  respectively (HM79). Heating due to formation of  $H_2$  on dust grains is given by

$$\Gamma_7 = 4.8 \times 10^{-29} n_H^2 f_{dust} x(H) \left(0.2 + \frac{4.2}{1 + n_{cr}/n_H}\right) \text{ ergs cm}^{-3} \text{ s}^{-1} \quad (\text{C8})$$

and  $f_{dust}$  is a factor that accounts for the change in dust surface area per  $H$  nucleus caused by changes in the size distribution and the gas-to-dust mass ratio as compared to interstellar values.

**Cosmic ray heating and other heating mechanisms** Apart from the processes discussed above, we consider cosmic ray heating ( $\Gamma_8$ ), photoionization of neutral carbon ( $\Gamma_9$ , see TH85), and heating by the excitation of [OI]63 $\mu\text{m}$  upper level by the IR continuum radiation field followed by the collisional de-excitation of this level ( $\Gamma_{10}$ , see Appendix D).

$$\Gamma_8 = 1.5 \times 10^{-11} \zeta n_H (x(H) + 2x(H_2)) \text{ ergs cm}^{-3} \text{ s}^{-1} \quad (\text{C9})$$

where  $\zeta$  is the primary cosmic ray ionization rate.

$$\Gamma_9 = 4.16 \times 10^{-29} n_H x(C) G_{11.26} \exp(-3A_v - \tau_{11.26}) \beta_C \text{ ergs cm}^{-3} \text{ s}^{-1} \quad (\text{C10})$$

where  $x(C)$  is the abundance of neutral carbon,  $\tau_{11.26}$  is the optical depth due to gas absorption towards the star in the FUV band that photoionizes carbon, and  $\beta_C$  is a self-shielding factor (van Dishoeck & Black 1988). To this term we also add similar terms for the contribution from the ISRF, and use optical depths and self-shielding factors due to gas columns vertically up and down from the spatial position in the disk.

#### D. Gas Cooling Processes

Gas cooling occurs by gas-grain collisions when the gas is warmer than the dust (Eq. C1) and by collisional excitation followed by line radiation of gaseous atoms, ions and molecules. We essentially follow the treatment of TH85, in which the cooling due to a transition from level  $i$  to level  $j$  is given by

$$\Lambda_{ij} = n_i A_{ij} h \nu_{ij} \beta_{esc}(\tau_{ij}) (1 - P(\nu_{ij})/S(\nu_{ij})) , \quad (D1)$$

where  $n_i$  is the population density of the species in level  $i$ ,  $A_{ij}$  is the spontaneous transition probability,  $h \nu_{ij}$  is the energy of the emitted photon,  $\tau_{ij}$  is the optical depth in the line and  $\beta_{esc}(\tau_{ij})$  is the associated escape probability.  $P(\nu_{ij})$  is the background radiation term which consists of the sum of the cosmic microwave background radiation and the infrared emission from the dust grains of different temperatures at the wavelength of the transition. The source function  $S(\nu_{ij})$  is determined by solving for the level populations assuming statistical equilibrium. We generally assume that radiation can escape from any point in the disk either vertically up or down or radially out the inner radius. We calculate the column densities in each level of the cooling species in all three directions. From the column densities we determine the optical depth in the line and the escape probability of a photon, which then gives the cooling rate in a given line. If the gas temperature is lower than that of dust, and the background radiation stronger than the source function, the transition can heat the gas as the term  $1 - P(\nu_{ij})/S(\nu_{ij})$  becomes negative. In this case, a background photon is absorbed by a particular species and subsequent collisional de-excitation transfers the excitation energy to gas heating.

We treat CO and H<sub>2</sub> cooling in a detailed multi-level calculation but treat OH and H<sub>2</sub>O somewhat differently. Analytical approximations to multi-level line cooling calculations of OH and H<sub>2</sub>O are derived for use in the gas disk code. The full level population calculation was prohibitively expensive to include in code and instead, we derived analytic fits for the total cooling similar to HM79. For H<sub>2</sub>O, we used collisional rate data for approximately 170 levels for both the ortho and para species, and new parameters (refer HM79) that best fit the data,  $\sigma = 2.0 \times 10^{-15} \text{ cm}^{-2}$ ,  $E_0/K = 23.0 \text{ K}$  and  $A_0 = 6.0 \times 10^{-3} \text{ s}^{-1}$ . The collisional

rate data for OH for the first 45 levels are used to obtain the values,  $\sigma = 8.0 \times 10^{-16} \text{ cm}^{-2}$ ,  $E_0/K = 5.4 \text{ K}$  and  $A_0 = 7.6 \times 10^{-4} \text{ s}^{-1}$ .

Table 5: Elemental gas phase abundances (from Savage & Sembach 1996)

Element	Abundance
He	0.1
C	$1.4 \times 10^{-4}$
O	$3.2 \times 10^{-4}$
Si	$1.7 \times 10^{-6}$
Mg	$1.1 \times 10^{-6}$
Fe	$1.7 \times 10^{-7}$
S	$2.8 \times 10^{-5}$

Table 6: Chemical species included in the models

H	He	C	O	H <sub>2</sub>	O <sub>2</sub>	OH	CO	H <sub>2</sub> O
H <sup>+</sup>	He <sup>+</sup>	C <sup>+</sup>	O <sup>+</sup>	OH <sup>+</sup>	CO <sup>+</sup>	H <sub>2</sub> O <sup>+</sup>	HCO <sup>+</sup>	H <sub>3</sub> O <sup>+</sup>
H <sub>2</sub> <sup>+</sup>	H <sub>3</sub> <sup>+</sup>	CH <sup>+</sup>	CH <sub>2</sub> <sup>+</sup>	CH <sub>3</sub> <sup>+</sup>	CH	CH <sub>2</sub>	Mg	Mg <sup>+</sup>
Si	Si <sup>+</sup>	SiH <sub>2</sub> <sup>+</sup>	SiH	SiO	Fe	Fe <sup>+</sup>	S	S <sup>+</sup>
SiO <sup>+</sup>	HOSi	H <sup>-</sup>		CH <sub>4</sub>	CH <sub>3</sub> CH <sub>4</sub> <sup>+</sup>	HS <sup>+</sup>	H <sub>2</sub> S <sup>+</sup>	H <sub>3</sub> S <sup>+</sup>
HS	H <sub>2</sub> S	CS	CS <sup>+</sup>	HCS <sup>+</sup> HCS	OCS	OCS <sup>+</sup>	HOCS <sup>+</sup>	
SO	SO <sup>+</sup>	HSO <sup>+</sup>	SO <sub>2</sub>	SO <sub>2</sub> <sup>+</sup> HSO <sub>2</sub> <sup>+</sup>	H <sub>2</sub> CS	H <sub>2</sub> CS <sup>+</sup>	H <sub>3</sub> CS <sup>+</sup>	
S <sub>2</sub> <sup>+</sup>	S <sub>2</sub> H <sup>+</sup>							

Table 7: Reaction rates where they differ from the UMIST'99 database.

H <sub>3</sub> O <sup>+</sup>	+	e <sup>-</sup>	→	H <sub>2</sub> O	+	H	4.0 × 10 <sup>-6</sup> $T^{-1/2}$
H <sub>3</sub> O <sup>+</sup>	+	e <sup>-</sup>	→	H <sub>2</sub>	+	H	+ O 1.73 × 10 <sup>-7</sup> $T^{-1/2}$
H <sub>3</sub> O <sup>+</sup>	+	e <sup>-</sup>	→	H <sub>2</sub>	+	OH	3.3 × 10 <sup>-6</sup> $T^{-1/2}$
H <sub>3</sub> O <sup>+</sup>	+	e <sup>-</sup>	→	OH	+	H	+ H 9.5 × 10 <sup>-6</sup> $T^{-1/2}$
H <sub>3</sub> <sup>+</sup>	+	e <sup>-</sup>	→	H <sub>2</sub>	+	H	2.9 × 10 <sup>-7</sup> $T^{-1/2}$
H <sub>3</sub> <sup>+</sup>	+	e <sup>-</sup>	→	H	+	H	+ H 9.0 × 10 <sup>-7</sup> $T^{-1/2}$
H	+	H	+	H	→	H <sub>2</sub>	+ H 8.8 × 10 <sup>-33</sup>
H <sub>2</sub>	+	H	+	H	→	H <sub>2</sub>	+ H <sub>2</sub> 2.8 × 10 <sup>-31</sup> $T^{-0.6}$

Table 8: Fits to photoionization cross sections where the cross section is given by  $\sigma_i(E) = \sigma_{0i}(E/1\text{keV})^\alpha$  and  $E_1 < E < E_2$ .

Atom	$\sigma_{0i}$ barns	$\alpha$	$E_1$ keV	$E_2$ keV
H	11.55	-3.4	0.5	10
He	43.12	-3.3	0.5	10
C	$4.56 \times 10^4$	-3.01	0.5	10
O	$7.34 \times 10^3$	-3.125	0.5	0.537
	$1.28 \times 10^5$	-2.9	0.537	10
Mg	$5.93 \times 10^4$	-2.38	0.5	1.312
	$5.5 \times 10^5$	-2.76	1.312	10
Si	$1.00 \times 10^5$	-2.44	0.5	1.835
	$9.12 \times 10^5$	-2.74	1.835	10
S	$1.686 \times 10^5$	-2.485	0.5	2.477
	$1.39 \times 10^6$	-2.7	2.477	10
Fe	$1.63 \times 10^5$	-1.98	0.5	0.726
	$2.075 \times 10^6$	-2.0	0.726	0.851
	$1.05 \times 10^6$	-2.52	0.851	7
	$6.67 \times 10^6$	-2.627	7	10

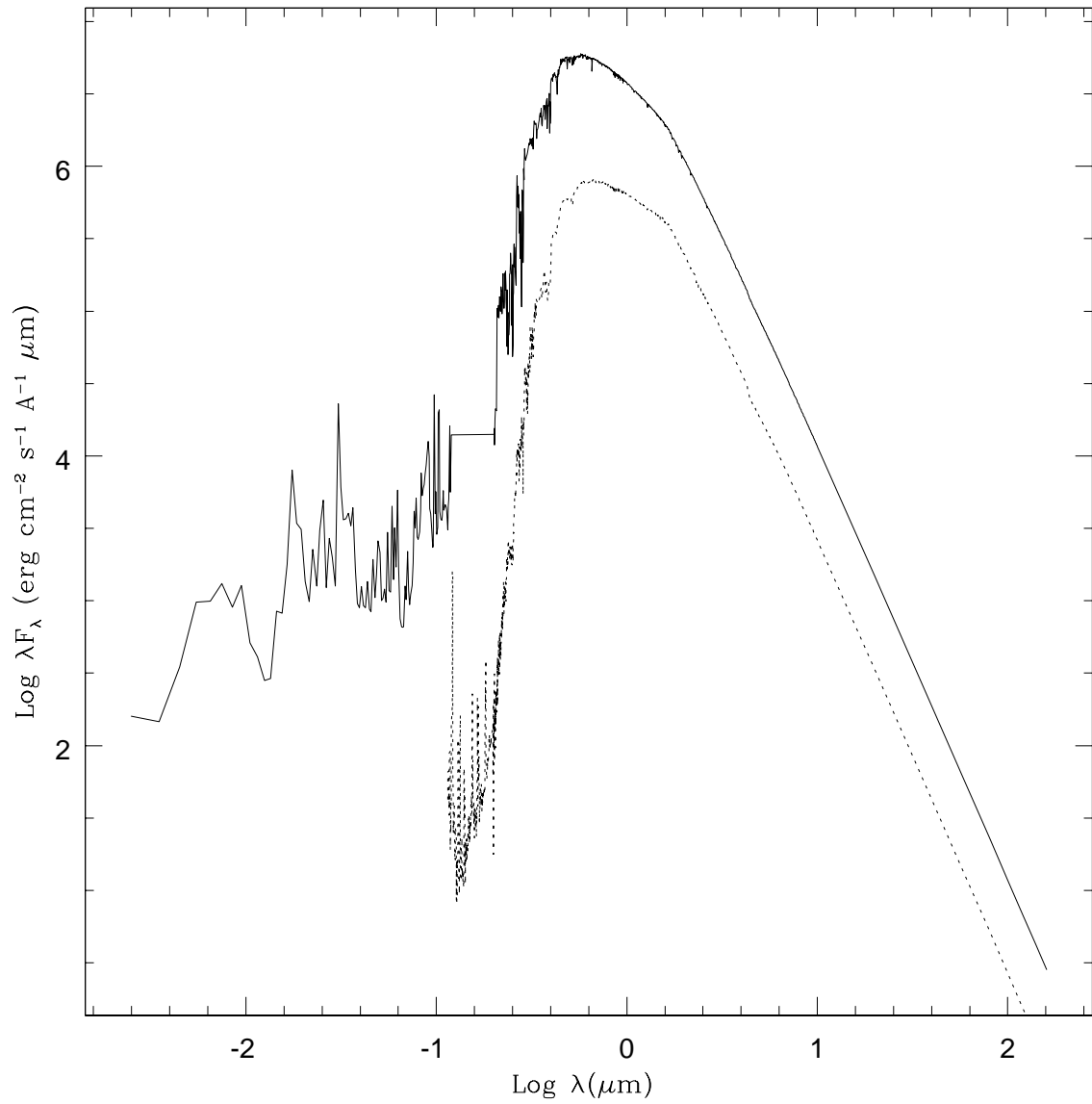


Fig. 1.— The adopted stellar spectrum for a 10 Myr old G2 star, consisting of an age-dependent UV flux added to a Kurucz model for the same spectral-type. The dashed line is a spectrum for a K star that includes chromospheric emission.

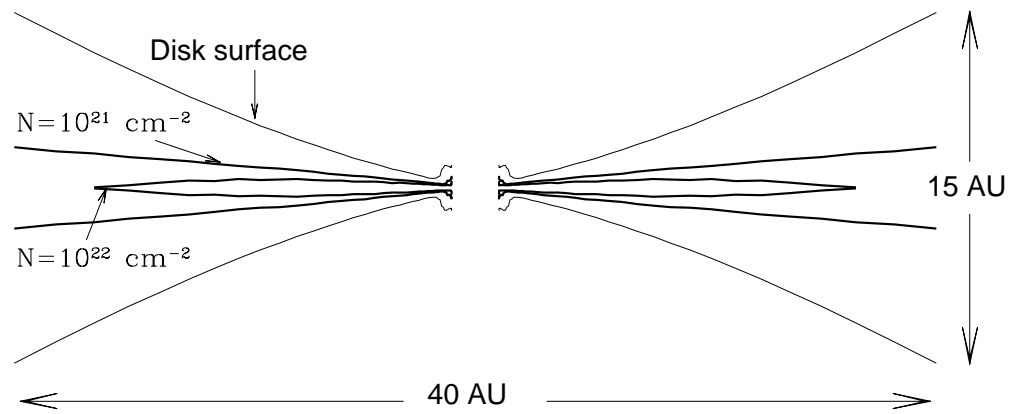


Fig. 2.— Disk surface for the standard case at a density equal to  $10^{-4}$  the density in the midplane, and contours that indicate surfaces where the vertical gas column densities to the surface are  $10^{21}$  and  $10^{22} \text{ cm}^{-2}$ .

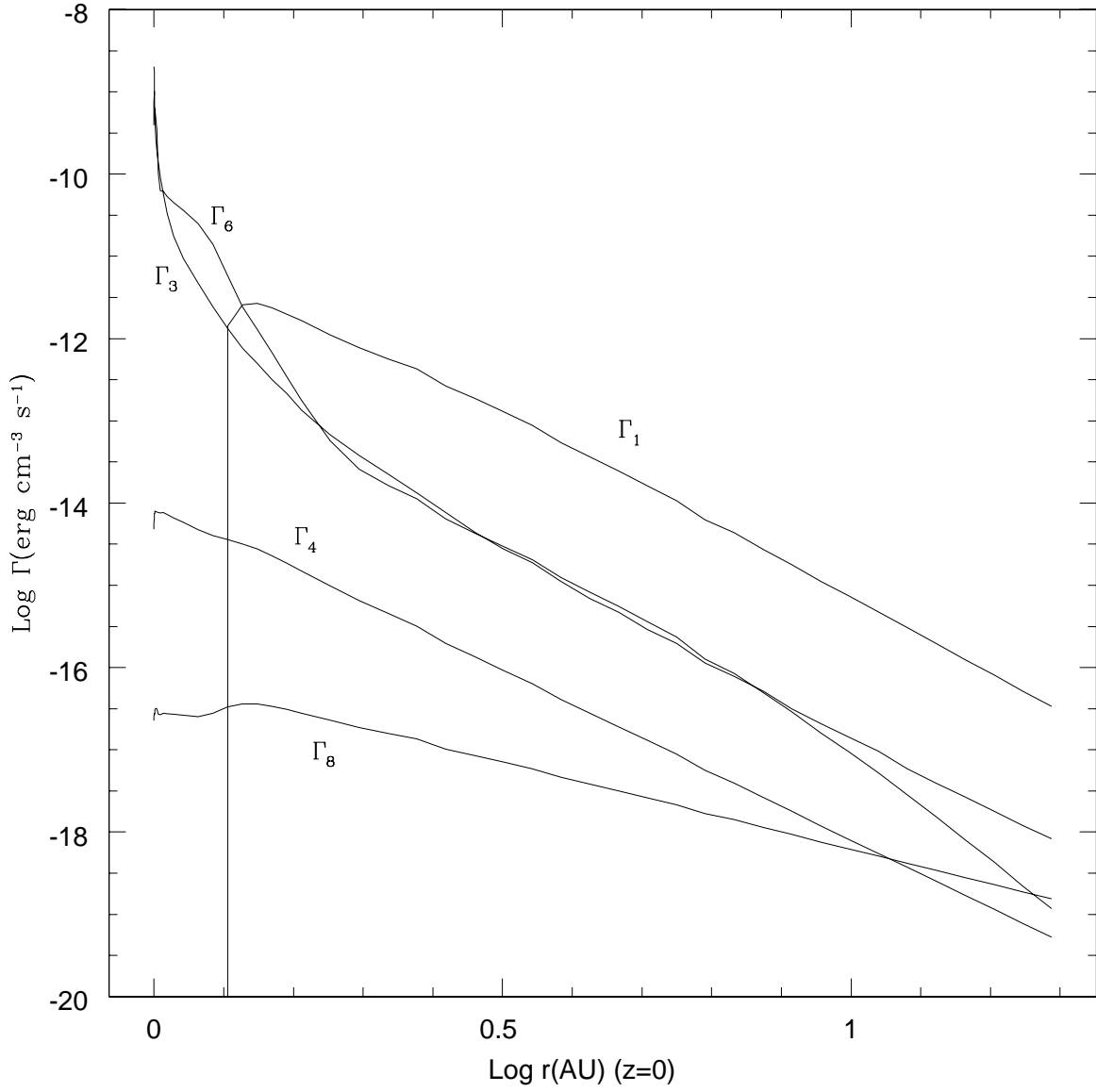


Fig. 3.— Heating terms as a function of radius in the disk midplane for the standard disk model with  $M_{gas} = 10^{-2} M_J$  and  $M_{dust} = 10^{-5} M_J$ .  $\Gamma_1$  is the heating due to gas-grain collisions,  $\Gamma_3$  is X-ray heating,  $\Gamma_4$  grain photoelectric heating,  $\Gamma_6$  heating due to  $H_2$  formation and  $\Gamma_8$  cosmic ray heating. See Appendix C for details.

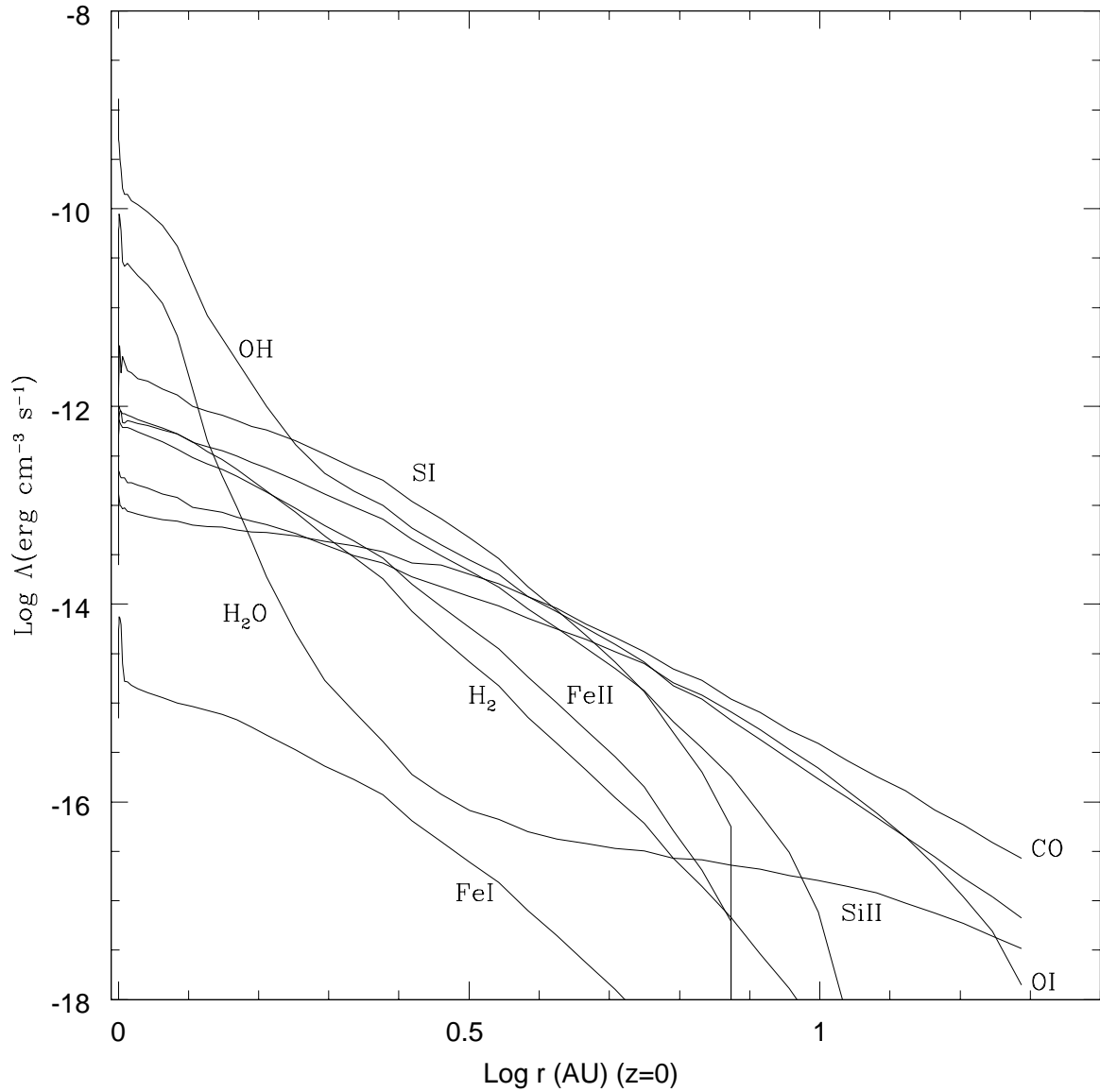


Fig. 4.— Cooling due to different chemical species as a function of radius in the disk midplane for the standard disk model.

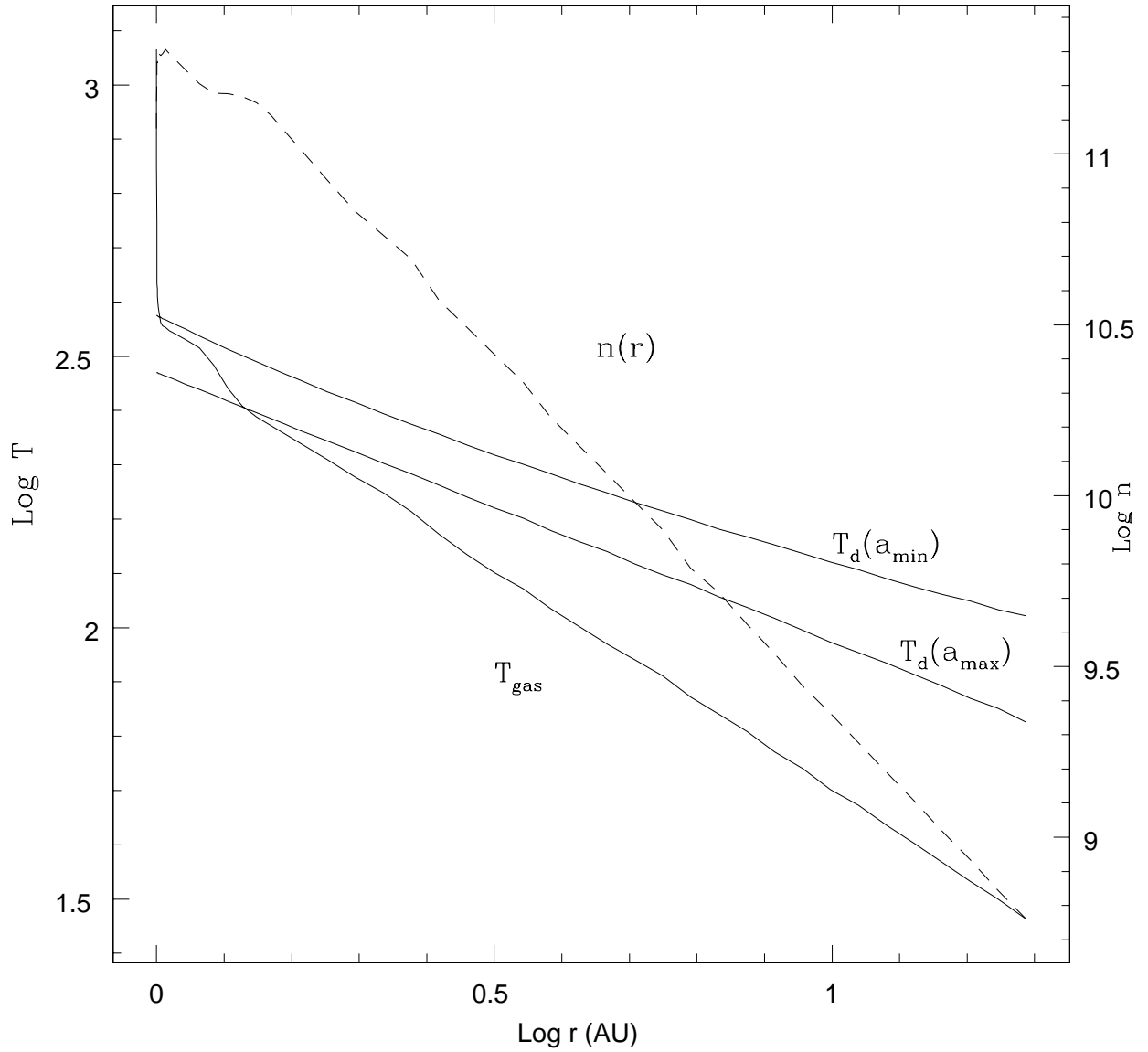


Fig. 5.— Gas and dust temperatures in the midplane of the disk are shown as (labelled) solid lines, whereas the dashed line shows the gas number density in the midplane for the standard disk model.

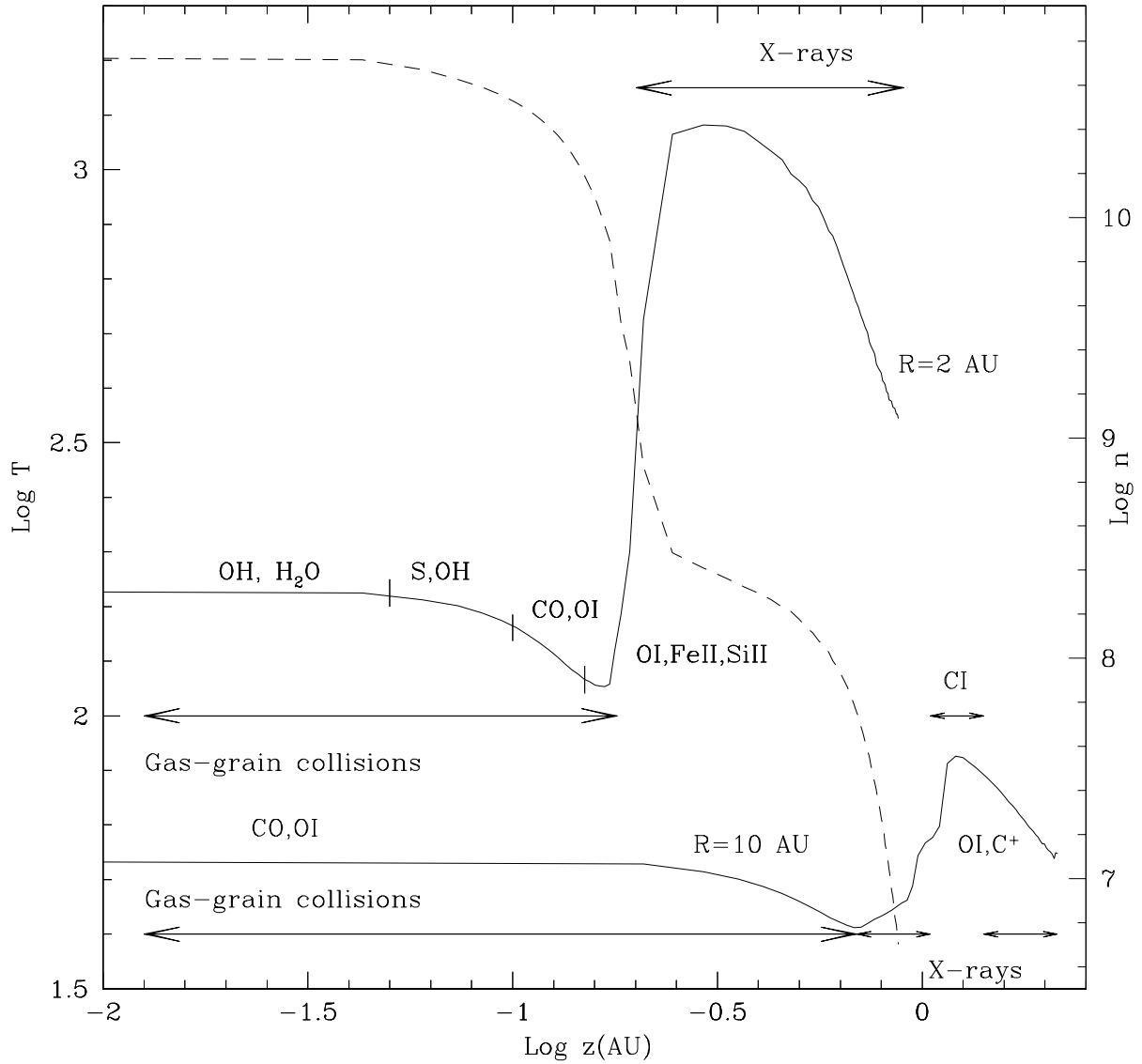


Fig. 6.— Gas temperature (solid line) and density (dashed line) as a function of  $z$  at a radial position of 2 AU and the temperature at 10 AU for the standard disk model. The dominant heating agents and the coolants in each region are marked on the temperature curve.

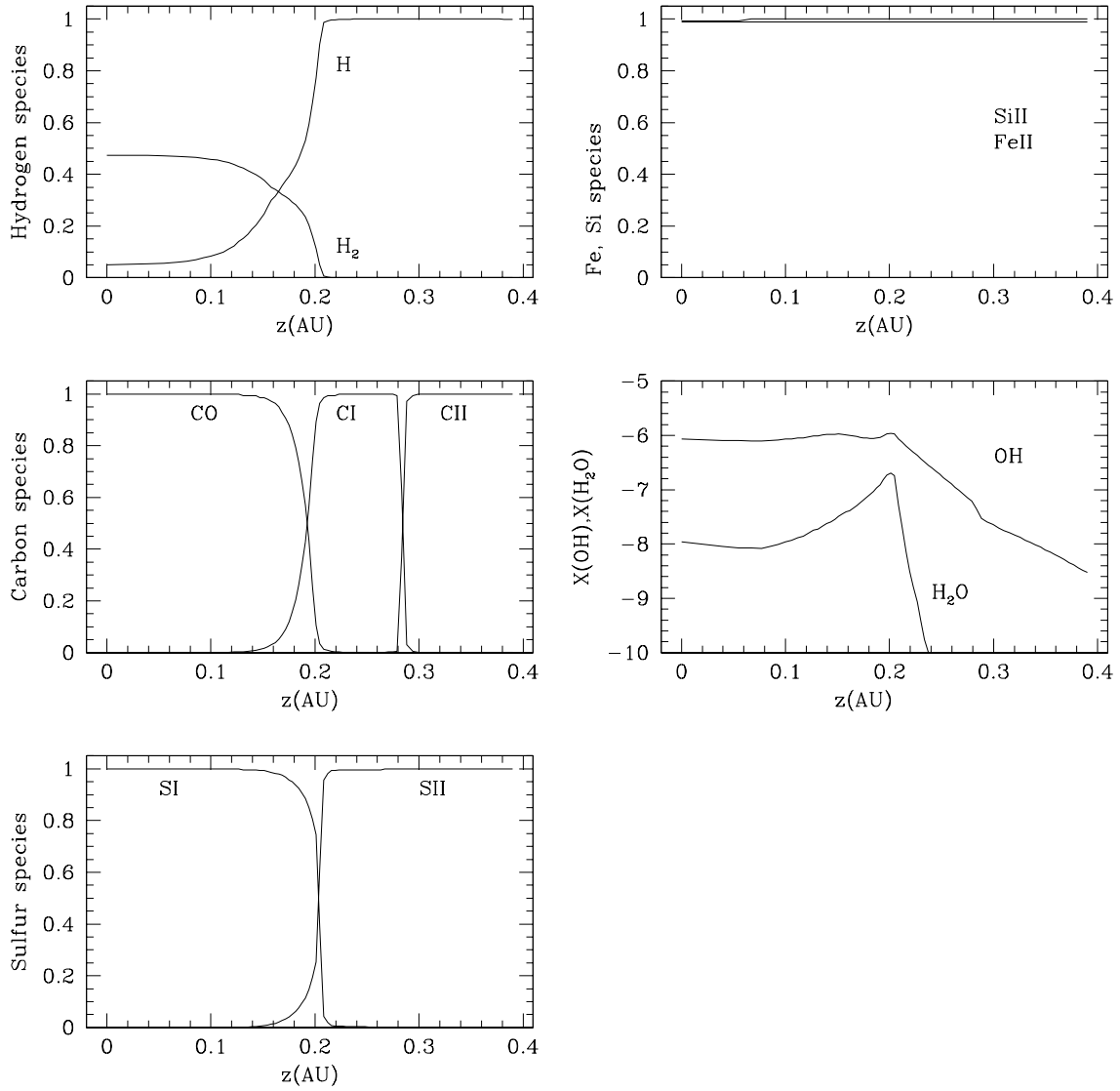


Fig. 7.— Abundances of important species as a function of  $z$  at a radius of 2 AU for the standard disk model. All abundances, except for OH and  $\text{H}_2\text{O}$ , have been normalized to their maximum possible values.

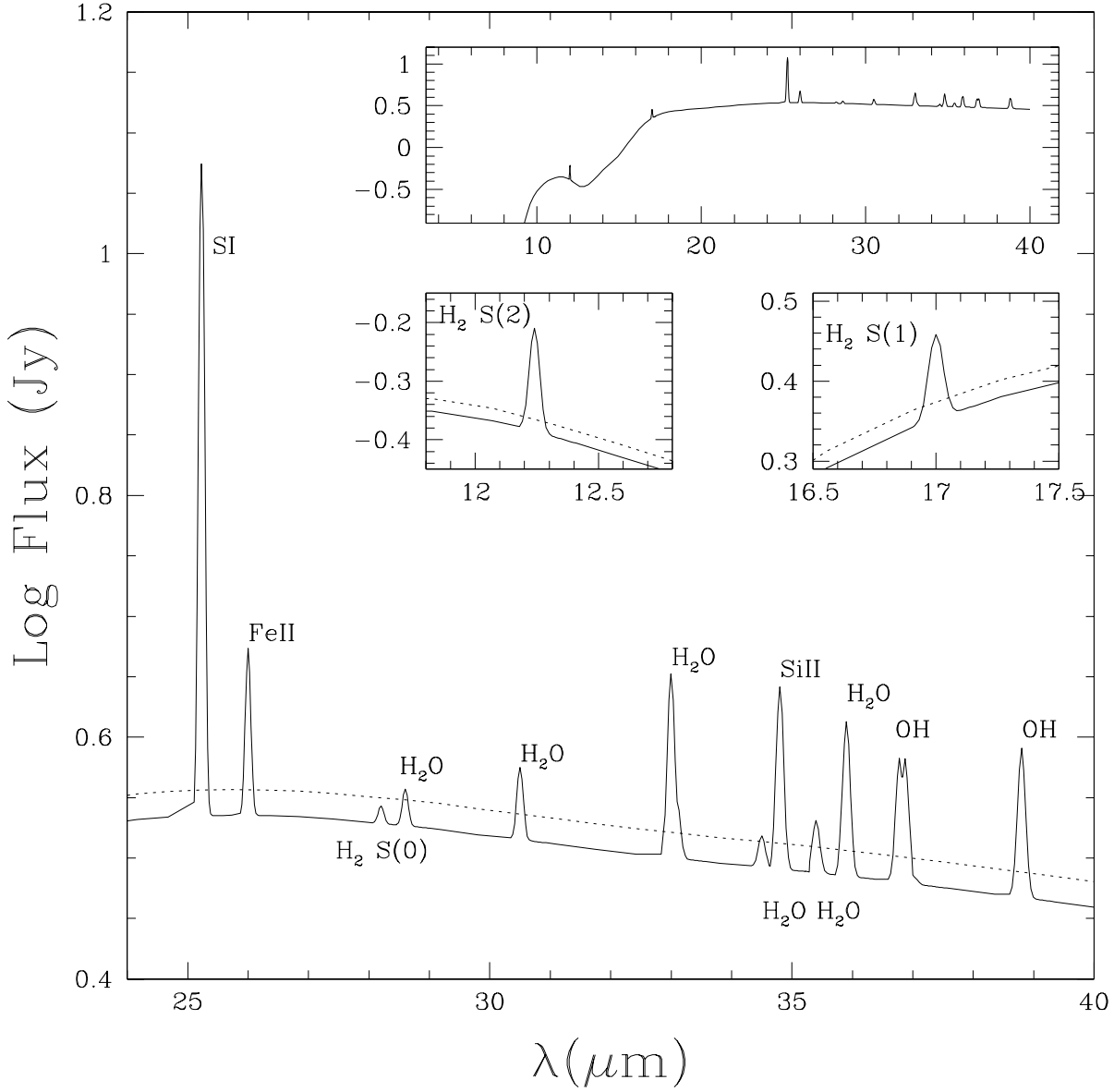


Fig. 8.— Mid-infrared spectrum in the 24–40  $\mu\text{m}$  wavelength region showing the dust continuum and dominant gas emission lines for the standard disk model, assuming a distance to the disk of 30 pc and a spectral resolving power  $(\lambda/\Delta\lambda)=600$ , typical of high resolution Spitzer observations. The dashed line indicates a 5% line-to-continuum ratio above which lines may possibly be detected. The insets show the complete spectrum from 10 – 40  $\mu\text{m}$ , and the  $\text{S}(1)$  and  $\text{S}(2)$  lines of  $\text{H}_2$ .

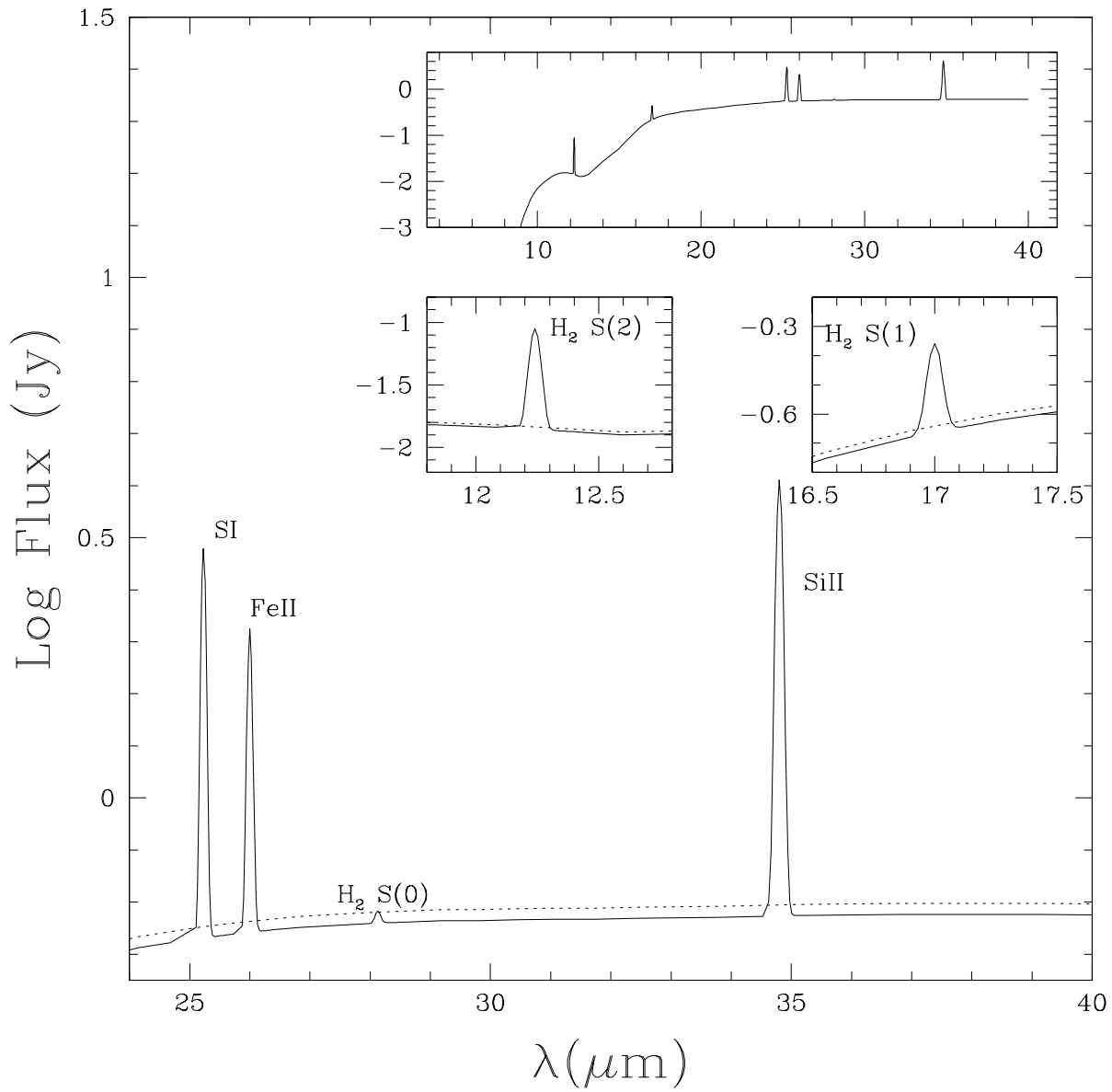


Fig. 9.— Mid-infrared spectrum (as in Figure 8), for a disk with an inner radius of 10 AU, and with all other parameters the same as the standard model.

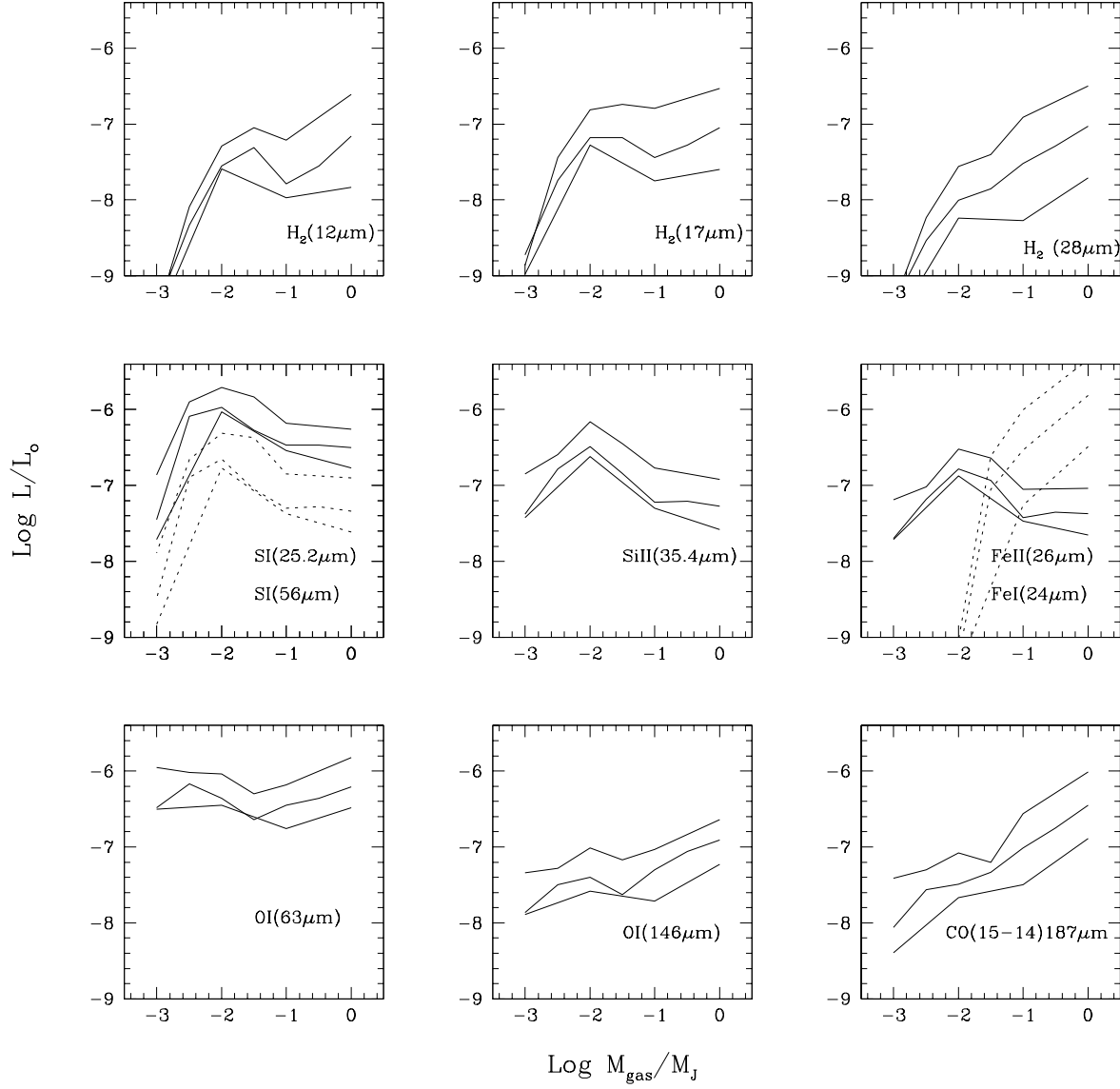


Fig. 10.— Mid-IR line luminosities as a function of disk gas mass, for different dust masses ( $10^{-5} M_J$  upper line,  $10^{-6} M_J$  middle line, and  $10^{-7} M_J$  lower line) in the disk. The dashed lines show the luminosities of the [SI]56 $\mu$ m line and the [FeI]24 $\mu$ m line.

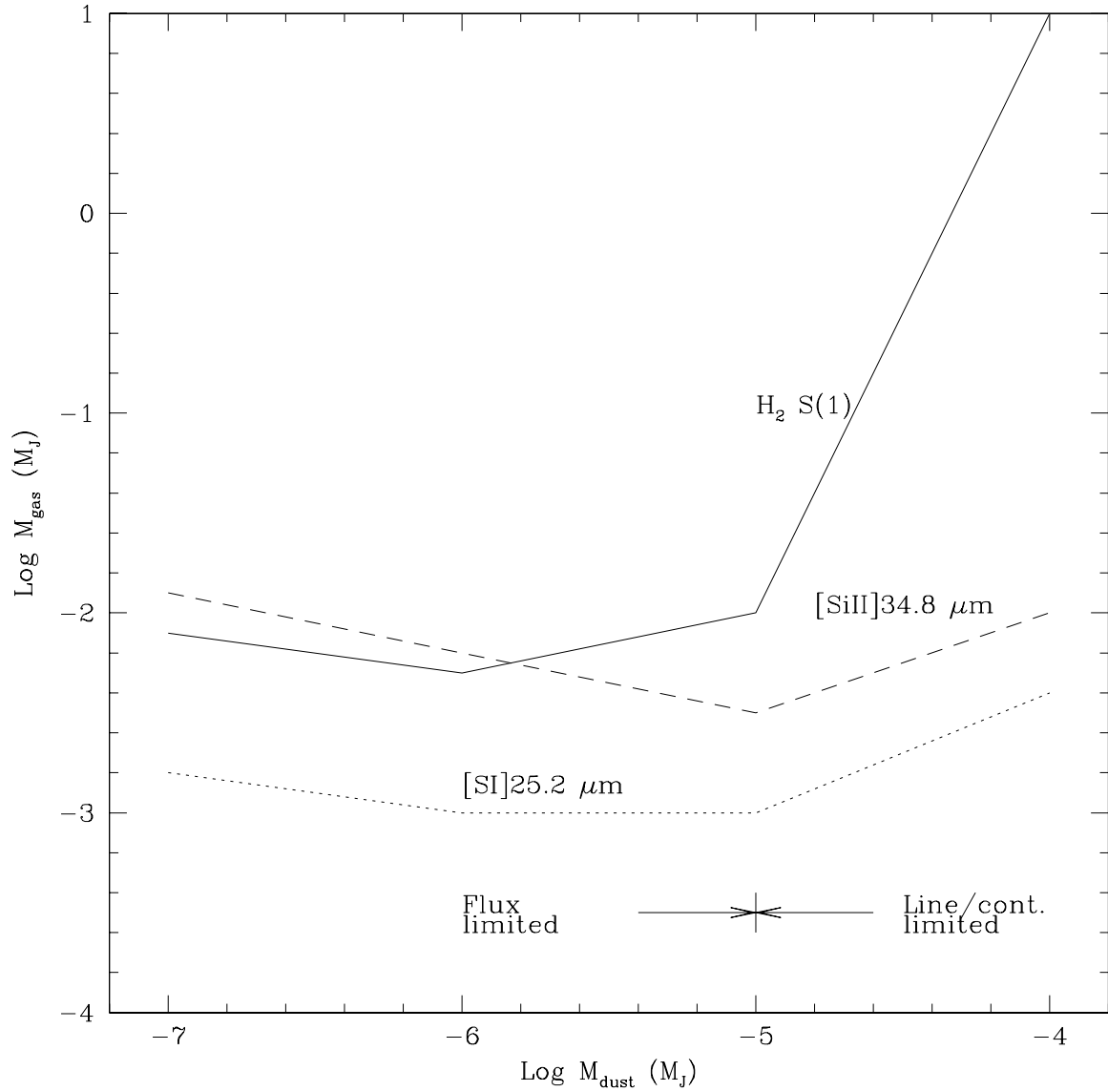


Fig. 11.— Detectability plots for three representative gas emission lines  $\text{H}_2 \text{ S}(1)$ ,  $[\text{Si}] 25.23 \mu\text{m}$  and  $[\text{SiII}] 34.8 \mu\text{m}$ , by the Spitzer Space Telescope (IRS instrument with  $R=600$ ) for a standard model disk at 30 pc. The lines show the minimum detectable gas mass for different dust masses in the disk for each line. For  $M_{\text{dust}} < 10^{-5} M_J$ , detection is flux limited ( $3 \times 10^{-8} L_\odot$  for  $\lambda \sim 25 \mu\text{m}$ ). For  $M_{\text{dust}} > 10^{-5} M_J$ , the line-to-continuum ratio is the limiting factor. We assume that a line-to-continuum ratio of 5% is sufficient for detection.

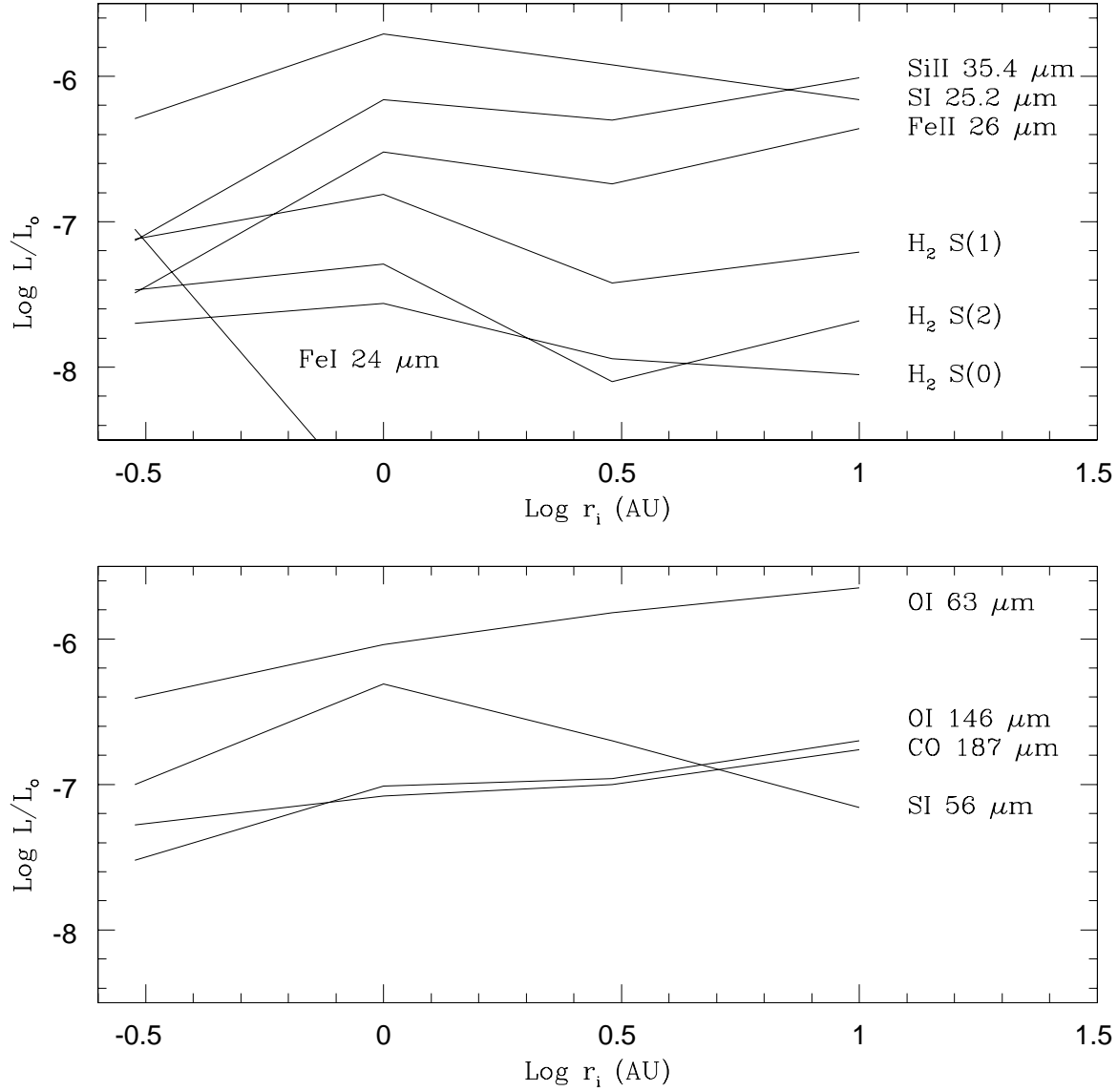


Fig. 12.— Gas line luminosities for disk models with differing inner radii,  $r_i$ , and other parameters as in the standard case.

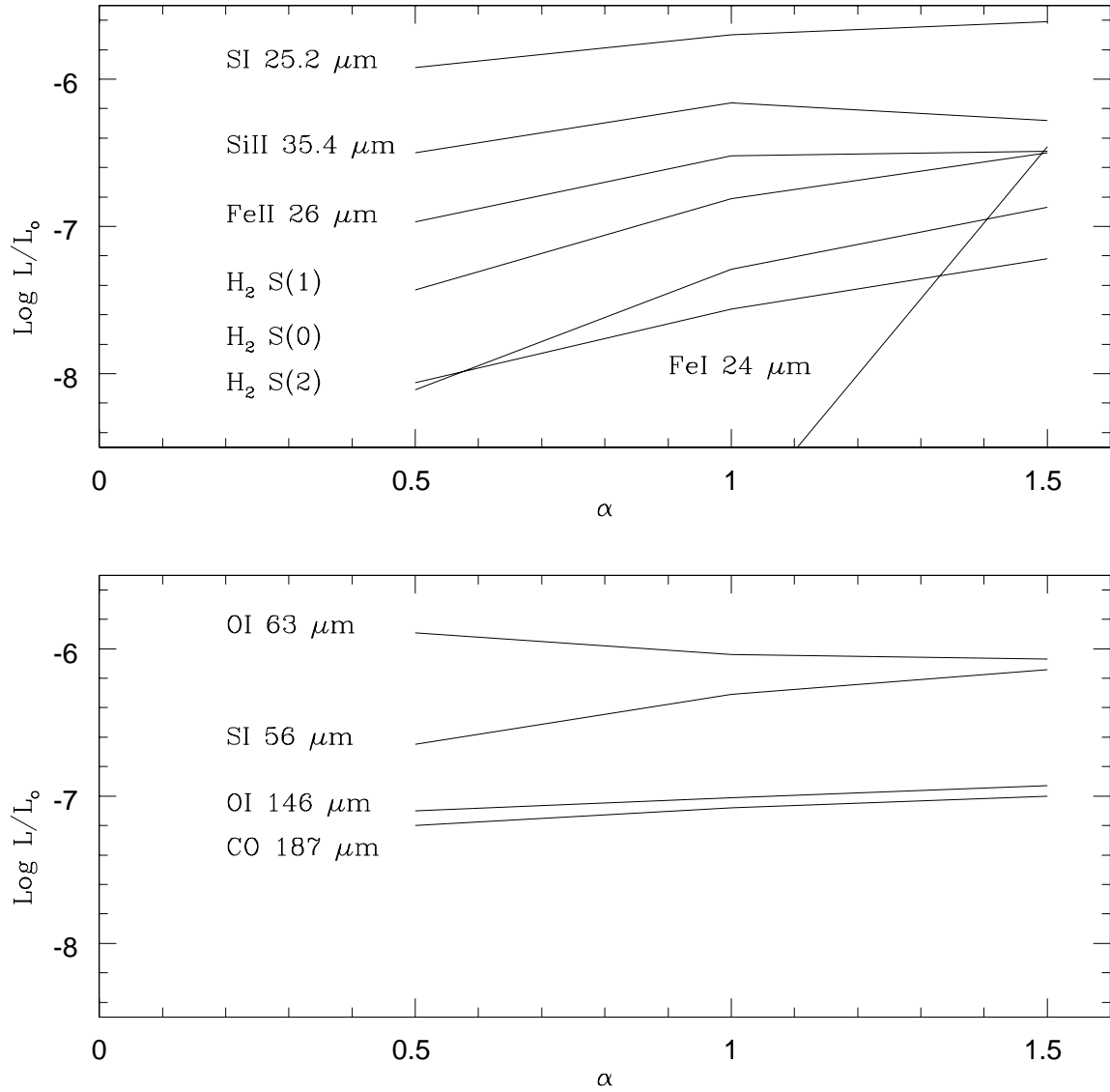


Fig. 13.— Changes in the line luminosities due to variations in the slope of the power law index  $\alpha$  of the surface density distribution.

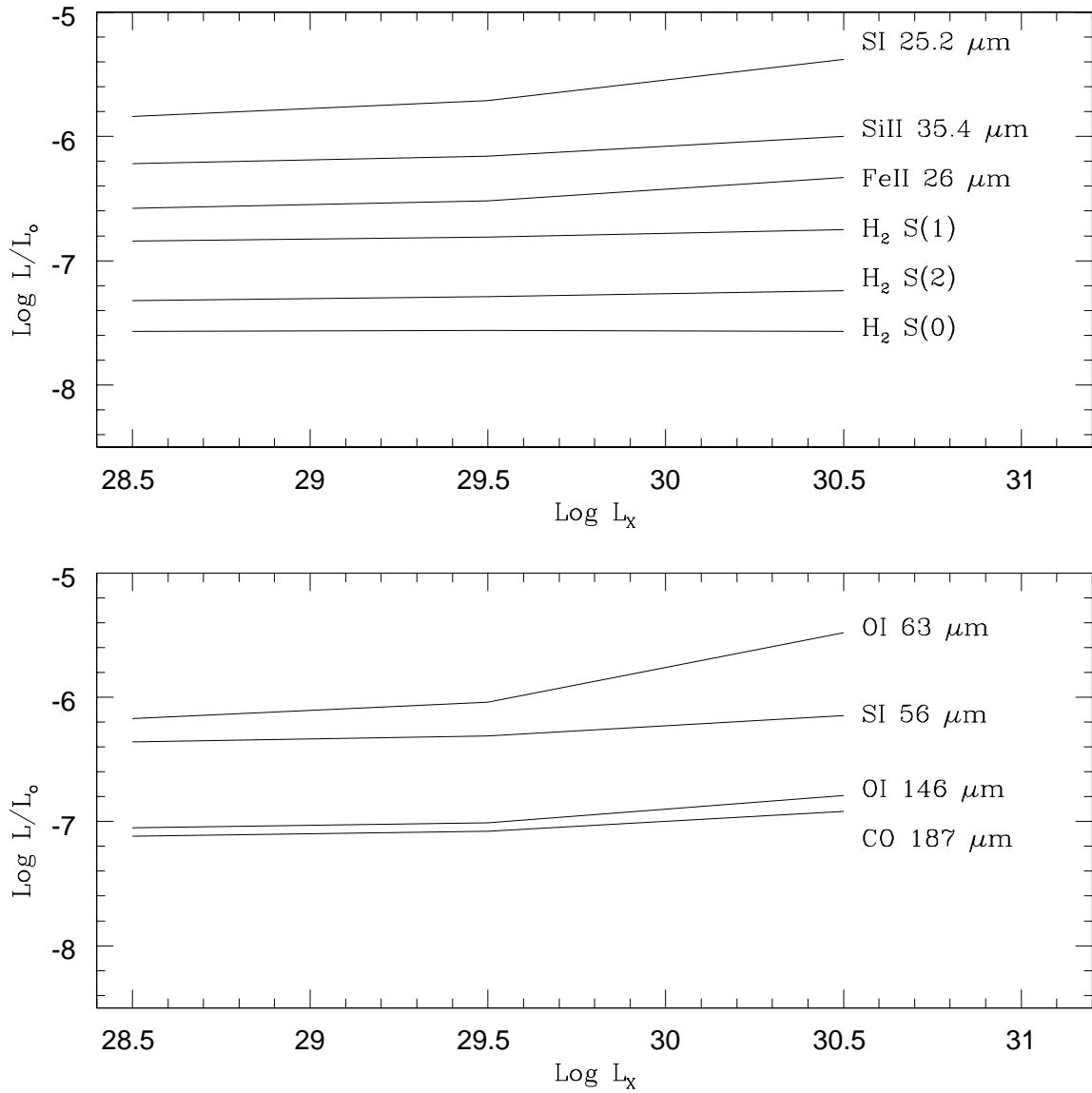


Fig. 14.— Gas line luminosities for disks around a G star with different X-ray luminosity.

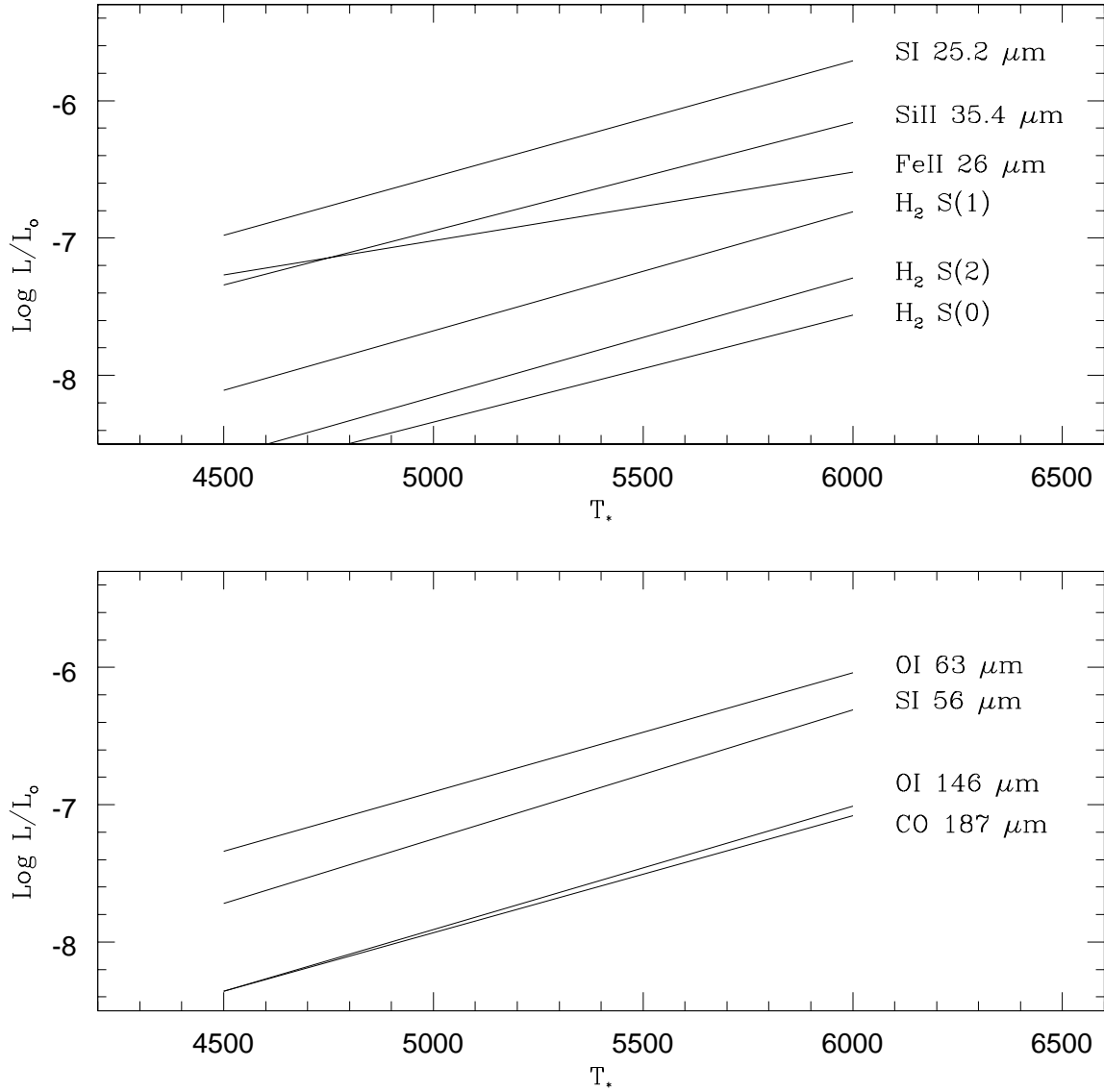


Fig. 15.— Gas line luminosities for disks with parameters as in the standard disk model but around a G star( $T_* = 6000$ ) and a K star( $T_* = 4500$ ).

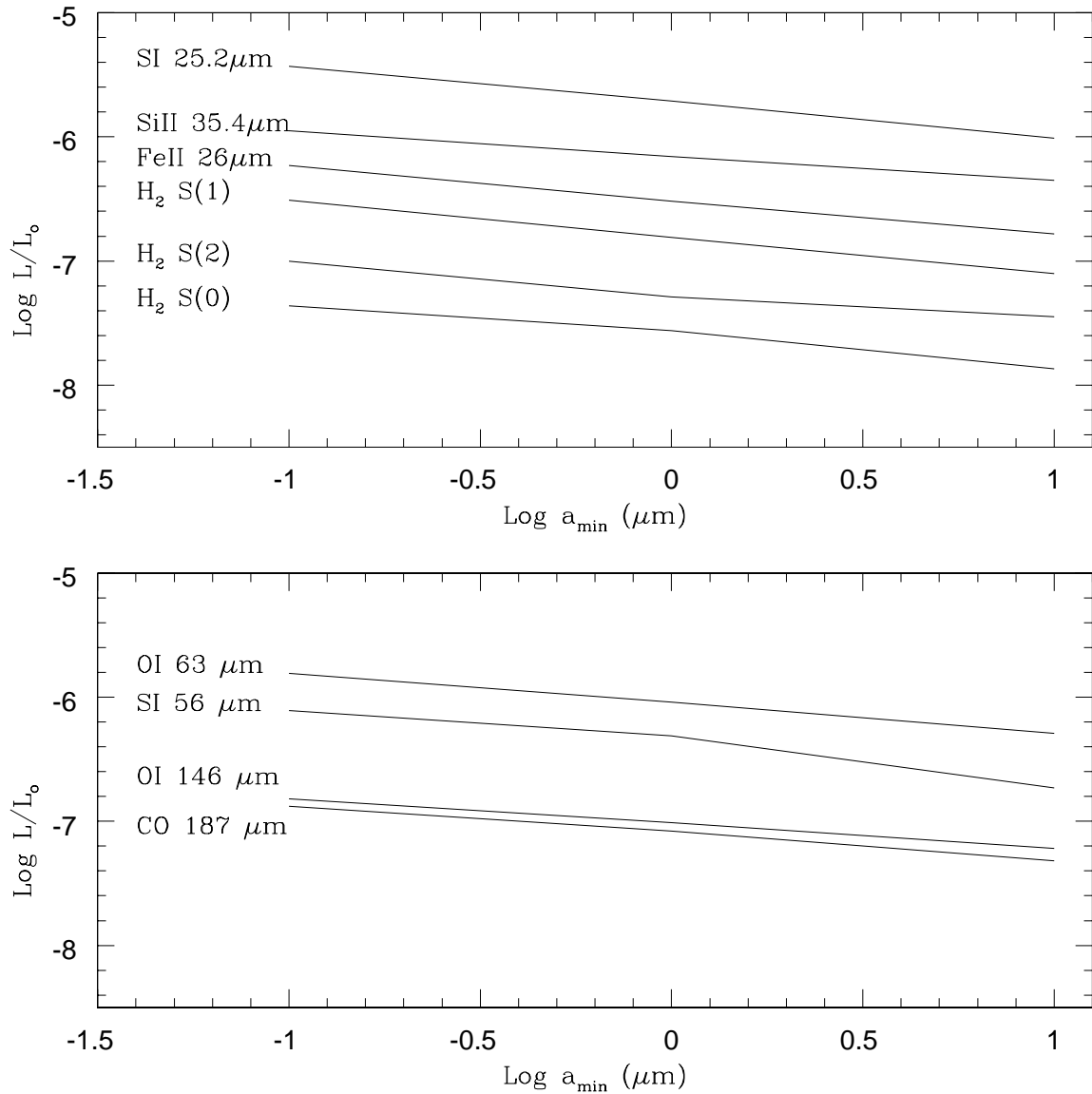


Fig. 16.— Gas line luminosities for disks with dust distributions where the minimum grain size  $a_{\min}$  is varied.